Deformable Open-Frame Cable-Driven Parallel Robots: Modeling, Analysis, and Control

Arthur Ngo Foon Chan, *Member, IEEE*, Wuichung Cheng, *Graduate Student Member, IEEE*, and Darwin Lau, *Senior Member, IEEE*

***Abstract*—This article proposes a generalized type of cable-driven parallel robot with deformable frames (D-CDPRs). The class of D-CDPRs allows: first, inevitable deformation of traditional rigid frame CDPRs to be considered; and second, new possibilities to develop CDPRs with lightweight frames that would deform. Comparatively, such lightweight CDPRs are easier to set up and largely reduce the cost of material and construction. However, the analysis and control of D-CDPRs are challenging as existing works usually assume the CDPR frame is rigid, such that the cable exit points on the frame are known and fixed. If the modeling errors induced by the deformable frame are not addressed appropriately, the control performance of D-CDPRs will be inaccurate and even unstable. To tackle this problem, novel modeling, analysis, and control approaches are proposed accordingly for D-CDPRs. Using the Euler–Bernoulli beam equations to develop a D-CDPR model, the workspace analysis is proposed and explored. Furthermore, the model-based feedforward length (MBFL) controller is proposed, where it is shown that cable length can be used to execute the tension control for D-CDPRs. Finally, the proposed work is validated in both simulation and hardware experiments.**

***Index Terms*—Deformable frame cable robots, flexible robots, parallel robots, tendon/wire mechanism.**

I. Introduction

CABLE-DRIVEN parallel robots (CDPRs) are a unique type of parallel mechanism, which utilize cables instead of rigid linkages [1]. Being the force transmitting medium between the end effector (EE) and the base frame, the set of cables maneuvers the EE via precise control of either cable tension (acceleration), velocity, or length. CDPRs exhibit numerous advantages over rigid-link parallel robots. Since cables are lightweight and easy to be deployed, CDPRs have favorable dynamic performance [2], [3], load-to-weight ratio [4], [5], and large scalable workspace [6], [7]. A wide range of applications have demonstrated the outstanding capability and versatility of CDPRs, including motion simulation [8], building construction [9], and the human walking characterization system [10].

Manuscript received 7 August 2023; revised 8 February 2024 and 11 May 2024; accepted 5 June 2024. Date of publication 28 June 2024; date of current version 17 July 2024. This work was supported by the Research Grants Council (General Research Fund Reference 14220822). This article was recommended for publication by Associate Editor M. Gouttefarde and Editor M. Yim upon evaluation of the reviewers' comments. *(Corresponding author: Darwin Lau.)*

The authors are with the Department of Mechanical and Automation Engineering, Chinese University of Hong Kong, Hong Kong SAR, China (e-mail: foonchan44@link.cuhk.edu.hk; 1155092902@link.cuhk.edu.hk; darwinlau@cuhk.edu.hk).

This article has supplementary downloadable material available at https://doi.org/10.1109/TRO.2024.3420714, provided by the authors.

Digital Object Identifier 10.1109/TRO.2024.3420714

Simplicity in the kinematic and dynamic modeling is a distinct advantage of CDPRs. However, the simplicity is achieved by satisfying several assumptions. First, cables are usually considered to be lightweight, such that the model of CDPRs can be simplified by neglecting the mass of cables. Second, it is assumed the positions of cables exit points are known [11], [12], [13], [14], [15]. The most common approach to ensure this is to assume that the robot frame structure is rigid. This implies that the frame would not deform under load, and hence, the cable exit points are accurately known.

Under the mentioned assumptions, the cable lengths and tension directions can be solved geometrically for a given EE's pose. Hence, the Jacobian matrix of CDPRs, which describes the velocity and force relationship between the joint space and task space, is a function of both the EE's pose and the exit points [16]. The Jacobian matrix is widely used in design [17], [18], [19], analysis [20], [21], [22], and control [23], [24], [25] of CDPRs. Under the rigid frame assumption where the exit points are known and fixed, the Jacobian matrix solely varies with the EE's pose. The CDPR's model can then be simplified by just considering the motion of EE and cable tensions.

The "rigid" frame assumption is typically achieved by constructing a sufficiently stiff frame that ensures negligible deformation during operation. High-stiffness frames can come in two different forms, closed frames and open frames. Closed frames have vertical and horizontal beams that are joined together to form a single structure. In contrast, open frames only have independent upright beams. Limitations and drawbacks result from attempting to fulfill the rigid frame assumption.

Although closed frames can be constructed with lighter material and less frame deformation by well-designed structures [26], [27], [28] compared with open frames, the volume of frame material and complexity would increase significantly as the robot becomes larger. Consequently, the material and construction costs of closed frames would escalate as the scale of CDPRs increased. For larger workspace applications, open frames are the more practical alternatives. For example, open frame CDPRs such as the FAST telescope [29] and the cooperative robot with multiple mobile cranes [30] are capable of enormous workspace. Nevertheless, as every individual cantilever beam has to withstand the cable tensions independently, the beams have to be significantly stiff to minimize deformation. This results in particularly large and heavy beams, leading to high material and construction costs.

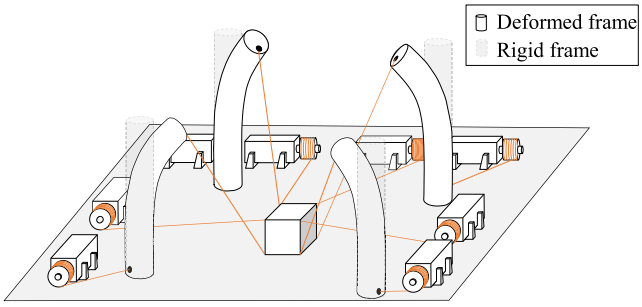

Fig. 1. Concept of deforming frame CDPR (D-CDPR).

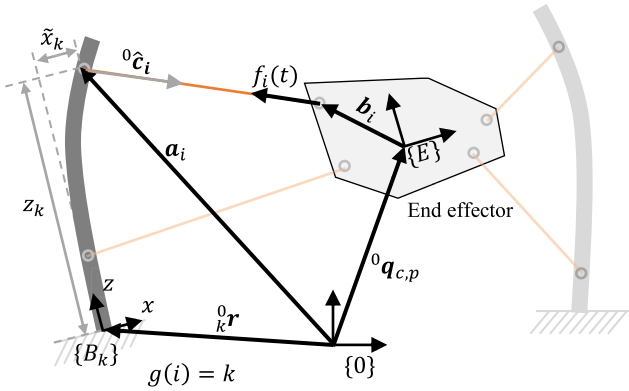

Fig. 2. Kinematics of a flexible frame CDPR.

However, despite the efforts to construct stiff frames, in reality, frames always deform under loading to a certain extent. Directly applying existing models and control approaches that neglect the frame dynamics and the motion of the cable exit points will result in significant errors in motion control and even control instability. A recent work proposed an elasto-static model for frame deformation [31], where the beam model is simplified as a rigid pole attached to a universal joint. However, both the dynamics of the deforming frame and the model for entirely flexible beams have never been studied before to the best of the authors' knowledge.

In this article, we propose a more generalized class of CDPRs that consider possible frame deformations through flexible beam frames, also known as D-CDPRs. When CDPRs with deformable frames (D-CDPRs) are used (see Fig. 1), the applied cable tensions would inevitably deform the frame, changing the position of the cable exit points and, thus, the cable force directions. This inherent coupled dynamic relationship between the EE and the deformable frame results in the nonlinear and uncertain behavior of the robot. To address the challenges raised by a deforming frame, a new D-CDPR dynamics model using Euler–Bernoulli (EB) beams [32] is proposed.

Based on the dynamics model, it is shown that the forward and inverse dynamics (ID) can be conveniently solved. In addition, existing static workspace (SW) and available wrench set (AWS) analyzes are extended to D-CDPRs, showing that the workspace and wrench generation capabilities change due to the deforming frame. Finally, a novel model-based feedforward length (MBFL) control approach using the D-CDPR model is proposed. More importantly, it is shown that for D-CDPRs, length commands can be used to produce desired cable tensions when the beam is attached to one cable. Simulation results on both planar and spatial D-CDPRs show that the proposed model can provide insight into the properties of D-CDPRs and that the proposed controller can achieve accurate trajectory tracking performance despite having a deforming frame. This result is then further validated on a planar D-CDPR hardware setup, where it is shown that the consideration of the deforming frame model significantly improves the tracking performance.

The proposed work is significant to the development of CDPRs for three purposes. First, all open frames are subject to some degree of frame deformation, traditional "rigid-frame" CDPRs that ignore frame deformation would result in some level of modeling error. Therefore, the proposed D-CDPR model would improve the performance of existing CDPRs, even when the deformation is small. Second, as larger frame deformation is allowable with the proposed approach, the requirement on the frame stiffness for CDPRs can be greatly reduced. As a result, the tolerance of deformation in the design of CDPRs' frame is significantly increased. Third, and most importantly, this work makes deformable materials and structures feasible options for CDPRs' frame. A new class of lightweight and more portable CDPRs, such as one constructed thin metal poles or plates, could emerge as practical CDPRs that could be deployed in the real-world in the future.

II. D-CDPR Kinematics and Dynamics

The pose of the CDPR EE can be defined as a set of generalized coordinates $\boldsymbol{q} \in \mathbb{R}^n$, where n is the degree-of-freedom (DoF) of the EE. For a spatial CDPR, the EE has 3 DoF in translation and 3 DoF in rotation, as represented as $\boldsymbol{q}_p$, $\boldsymbol{q}_r \in \mathbb{R}^3$, respectively. Suppose the frame of the CDPR is deforming with time, the state of the frame is represented by the state variable $\boldsymbol{\eta}(t)$.

The ith cable vector $\boldsymbol{c}_i$ is defined as a vector pointing from the ith frame cable outlet ${}^0\boldsymbol{a}_i$ to the corresponding EE anchor point ${}^E\boldsymbol{b}_i$, as shown in Fig. 2. It will be assumed that the EE is rigid and does not deform, and hence, the anchor points are fixed with respect to the EE frame $\{E\}$. The ith cable vector $\boldsymbol{c}_i$ with respect to the inertial frame $\{0\}$ could be defined as

$$ {}^0\boldsymbol{c}_i = \boldsymbol{q}_p - {}^0\boldsymbol{a}_i(\boldsymbol{\eta}) + {}^0_E\mathbf{R}(\boldsymbol{q}_r)\,{}^E\boldsymbol{b}_i \tag{1} $$

where ${}^0_E\mathbf{R}(\boldsymbol{q}_r)$ is the rotation matrix between frame $\{E\}$ and $\{0\}$. It is worth noting that the exit points $\boldsymbol{a_i}$ of a D-CDPR depend on the frame's state.

The equation of motion (EoM) of the EE of the D-CDPR can be expressed in the form

$$ \mathbf{M}(\boldsymbol{q})\ddot{\boldsymbol{q}} + \mathbf{C}(\boldsymbol{q}, \dot{\boldsymbol{q}}) + \boldsymbol{g}(\boldsymbol{q}) + \boldsymbol{w}_{\text{ext}} = \mathbf{W}(\boldsymbol{q}, \boldsymbol{\eta})\boldsymbol{\tau} \tag{2} $$

where $\mathbf{M} \in \mathbb{R}^{n\times n}$, $\mathbf{C} \in \mathbb{R}^n$, $\boldsymbol{g} \in \mathbb{R}^n$, and $\boldsymbol{w}_{\text{ext}} \in \mathbb{R}^n$ are the mass-inertia matrix, centrifugal and Coriolis vector, gravity vector, and external wrench vector, respectively. The cable tension

vector $\boldsymbol{\tau} = [\tau_1, \tau_2, \ldots, \tau_m]^T \in \mathbb{R}^m_+$ is a nonnegative real number set of all cable tension as the cable cannot be compressed. Matrix $\mathbf{W} \in \mathbb{R}^{n\times m}$ is the wrench matrix [33] that maps the joint wrench space into cable tension space. Without lost of generality, for a spatial CDPR

$$\mathbf{W} = -\begin{bmatrix} {}^0\hat{\boldsymbol{c}}_1 & \cdots & {}^0\hat{\boldsymbol{c}}_m \\ ({}^0_E\mathbf{R}^E\boldsymbol{b}_1)\times{}^0\hat{\boldsymbol{c}}_1 & \cdots & ({}^0_E\mathbf{R}^E\boldsymbol{b}_m)\times{}^0\hat{\boldsymbol{c}}_m \end{bmatrix} \tag{3}$$

where ${}^0\hat{\boldsymbol{c}}_i$ is the unit vector of ith cable vector (1), which depends on both the CDPR EE's pose $\boldsymbol{q}$ and cable exit points $\boldsymbol{a}$, as shown in Fig. 2.

The basic framework of this work involves considering the dynamics of the frame, bringing about a change in perspective. It is supposed that the dynamics of the frame can be described by a second-order ordinary differential equation (ODE) as follows:

$$\mathbf{M}_b(\boldsymbol{\eta})\ddot{\boldsymbol{\eta}} + \boldsymbol{c}_b(\boldsymbol{\eta}, \dot{\boldsymbol{\eta}}) + \boldsymbol{k}_b(\boldsymbol{\eta}) = \boldsymbol{f}_b(\boldsymbol{\tau}). \tag{4}$$

The matrix $\mathbf{M_b}$ depends on $\boldsymbol{\eta}$ and multiplies with $\ddot{\boldsymbol{\eta}}$. The vector $\boldsymbol{c}_b$ groups the terms related to $\dot{\boldsymbol{\eta}}$, while $\boldsymbol{k}_b$ groups the remaining terms. On the left-hand side of (4), $\boldsymbol{f}_b$ represents the external force applied to the frame. For D-CDPR, this force depends on the cable tension $\boldsymbol{\tau}$.

To express the dynamics of the CDPR and frame system simultaneously, one can combine (2) and (4) as follows:

$$\begin{cases} \mathbf{M}(\boldsymbol{q})\ddot{\boldsymbol{q}} + \mathbf{C}(\dot{\boldsymbol{q}}, \boldsymbol{q}) + \boldsymbol{g}(\boldsymbol{q}) = \mathbf{W}(\boldsymbol{q}, \boldsymbol{\eta})\boldsymbol{\tau} \\ \mathbf{M}_b(\boldsymbol{\eta})\ddot{\boldsymbol{\eta}} + \boldsymbol{c}_b(\boldsymbol{\eta}, \dot{\boldsymbol{\eta}}) + \boldsymbol{k}_b(\boldsymbol{\eta}) = \boldsymbol{f}_b(\boldsymbol{\tau}). \end{cases} \tag{5}$$

Please note that the exit points of a D-CDPR are dependent on the state of the frame $\boldsymbol{\eta}$, which means that the wrench matrix $\mathbf{W}$ also depends on $\boldsymbol{\eta}$.

III. Forward Dynamics (FD) of D-CDPR With EB Model

In this section, the deformation behavior of the vertical pole can be analyzed by modeling the cantilever beam dynamics. The EB beam theory, along with the Euler–Lagrange equations, is a suitable candidate for this work as only small deflection is considered. A numerical approximation using the Galerkin Method will be presented to approximate the deformation of both 1-D and 3-D beam dynamics models. This allows the partial differential equation to be transformed into discretized ODEs and fitted into (5). By combining the EB beam theory with the Galerkin method, the model retains a certain degree of accuracy without excessive use of variables. Lastly, the kinematic and dynamic relation of D-CDPR with EB beam model would be expressed.

A. Deflection Dynamics of a 1-D Beam by Galerkin Method

Consider a one-dimensional beam with length L fixed along with an arbitrary z-axis with respect to the $\{B\}$ frame. Without loss of generality, two ends of the beam are located at $z = 0$ and $z = L$. For a transverse load $d_x(z, t)$, which is a function of both position and time, the beam would deflect to the same direction as the load. The deflection $\tilde{x}$ of the beam at z and time t can be described by the function $\tilde{x}(z, t)$. According to the Euler–Lagrange equation, the dynamics of the beam can be expressed as

$$\frac{\partial^2}{\partial z^2}\left(\mathrm{EI}\frac{\partial^2\tilde{x}}{\partial z^2}\right) + \rho A\frac{\partial^2\tilde{x}}{\partial t^2} = d_x(z, t) \tag{6}$$

where E, I, ρ, and A are the Young's modulus, second moment of area, density, and cross sectional area of the beam, respectively, all measured along the x-direction.

To solve the abovementioned fourth-order (6), four boundary equations are needed. Suppose the fixed end (position and slope is fixed) of the cantilever beam is at $z = 0$, then the first two boundary conditions are

$$\tilde{x}\big|_{z=0} = 0 \quad \frac{\partial\tilde{x}}{\partial z}\bigg|_{z=0} = 0. \tag{7a}$$

At the free end $z = L$, there is no bending moment and shear force, hence, the another two the boundary conditions are

$$\frac{\partial^2\tilde{x}}{\partial z^2}\bigg|_{z=L} = 0 \quad \frac{\partial^3\tilde{x}}{\partial z^3}\bigg|_{z=L} = 0. \tag{7b}$$

Note that (6) assumes that the cross-section of the beam does not deform in a significant manner, where it remains planar and normal to the bent axis during deformation. The superposition principle is applied when there are multiple loads to the beam.

The partial differential equation (6) can be converted into discretized ODE by the Galerkin method, of which the deflection function can be approximated as $\tilde{x}(z, t) \approx \tilde{x}_a(z, t)$ and

$$\tilde{x}_a(z, t) = \sum_{i=1}^{N} \phi_i(z)\eta_{x,i}(t) = \boldsymbol{\phi}^T(z)\boldsymbol{\eta}_x(t) \tag{8}$$

where N is the order of discretization, $\phi_i(z)$ are the predetermined comparison functions that satisfy all boundary conditions. The symbol $\boldsymbol{\phi}(z) : \mathbb{R} \to \mathbb{R}^N$ is a vector-valued function that stores all the comparison functions $\boldsymbol{\phi}(z) = [\phi_1(z) \ldots \phi_N(z)]^T$. One comparison function could be the eigenfunctions of the cantilever beam

$$\begin{aligned} \phi_i(z) = {} & \cosh\beta_i z - \cos\beta_i z \\ & + \frac{\cos\beta_i L + \cosh\beta_i L}{\sin\beta_i L + \sinh\beta_i L}(\sin\beta_i z - \sinh\beta_i z) \end{aligned} \tag{9}$$

where β_i is the ith solutions of the equation

$$\cosh\beta_i L \ \cos\beta_i L + 1 = 0. \tag{10}$$

As shown in (8), each comparison function is multiplied with a time-dependent coefficient $\eta_{x_i}(t)$. The vector $\boldsymbol{\eta}_x(t) = [\eta_{x_1}(t) \ldots \eta_{x_N}(t)]^T$ stores all coefficients. Substituting $\tilde{x}_a$ into (6) results in

$$\frac{\partial^2}{\partial z^2}\left(\mathrm{EI}\frac{\partial^2\tilde{x}_a}{\partial z^2}\right) + \rho A\frac{\partial^2\tilde{x}_a}{\partial t^2} \approx d_x(z, t). \tag{11}$$

A residual function $\varepsilon(z)$ represents the difference between the actual transverse load (6) and the approximated transverse load (11) and can be defined as

$$\varepsilon(z, t) = \frac{\partial^2}{\partial z^2}\left(\mathrm{EI}\frac{\partial^2\tilde{x}_a}{\partial z^2}\right) + \rho A\frac{\partial^2\tilde{x}_a}{\partial t^2} - d_x(z, t). \tag{12}$$

Substituting (8) into (12) results in

$$\begin{aligned}\varepsilon =& \left(\mathrm{EI}(\boldsymbol{\phi}^T\boldsymbol{\eta}_x)^{(2)}\right)^{(2)} + \rho A\frac{\partial^2}{\partial t^2}(\boldsymbol{\phi}^T\boldsymbol{\eta}_x) - d \\ =& \eta_{x,i}\sum_{i=1}^{N}\left[(\mathrm{EI})^{(2)}\phi_i^{(2)} + 2(\mathrm{EI})^{(1)}\phi_i^{(3)} + (\mathrm{EI})\phi_i^{(4)}\right] \\ &+ \ddot{\eta}_{x,i}\rho A\sum_{i=1}^{N}\phi_i - d \end{aligned} \tag{13}$$

where $g^{(n)}(z)$ is the nth derivative of function $g(z)$ with respect to z. According to the Galerkin method, the residual (error) is to be minimized by forcing the inner product of two functions to be zero. Mathematically, this can be expressed as

$$\langle \varepsilon, \phi_j \rangle = \int_0^L \varepsilon\phi_j dz = 0,\ j = 1, \ldots, N. \tag{14}$$

Substituting (13) into (14) results in the EoM by factorizing the coefficient η_x and its derivative

$$\mathbf{M}_{b,x}\ddot{\boldsymbol{\eta}}_x + \mathbf{K}_{b,x}\boldsymbol{\eta}_x = \boldsymbol{f}_{b,x} \tag{15}$$

where the matrices $\mathbf{M}_{b,x}, \mathbf{K}_{b,x} \in \mathbb{R}^{N\times N}$ are analogous to the mass and stiffness matrices, respectively. The vector $\boldsymbol{f}_{b,x}$ is analogous to the external force vector. The entries of these quantities can be expressed as

$$M_{b,x,ij} = \int_0^L \rho A\phi_i\phi_j dz \tag{15a}$$

$$K_{b,x,ij} = \int_0^L \left[(\mathrm{EI})^{(2)}\phi_i^{(2)} + 2(\mathrm{EI})^{(1)}\phi_i^{(3)} + \mathrm{EI}\phi_i^{(4)}\right]\phi_j dz \tag{15b}$$

$$f_{b,x,i} = \int_0^L d_x(z,t)\phi_i dz, \qquad i,j = 1, \ldots, N. \tag{15c}$$

The solution to $\boldsymbol{\eta}_x(t)$ to (15) would allow the beam deflection in 1-D, $\tilde{x}_a(z,t)$ to be determined as expressed in (8).

B. Deflection Dynamics Under Multiple External 3-D Forces

The beam deflection due to an arbitrary point force in 3-D space will now be considered. Suppose a reference frame $\{B\}$ has three orthogonal axes, namely x, y, and z, as shown in Fig. 3. Any arbitrary direction time-varying 3-D point force ${}^0\boldsymbol{p}(t)$ with respect to the inertial frame $\{0\}$ acting on the beam can thus be represented in $\{0\}$ by

$${}^B\boldsymbol{p}(t) = {}^B_0\mathbf{R}\,{}^0\boldsymbol{p}(t). \tag{16}$$

Due to the EB beam assumption, the axial force component (in z-axis) will be neglected. The force component in x and y axes would cause the beam to deflect in x and y directions, respectively.

Representing the x-component point force ${}^Bp_x(t)$ as a distributed load $d_x(z,t)$ by

$$d_x(z,t) = {}^Bp_x(t)\delta(z - z') \tag{17}$$

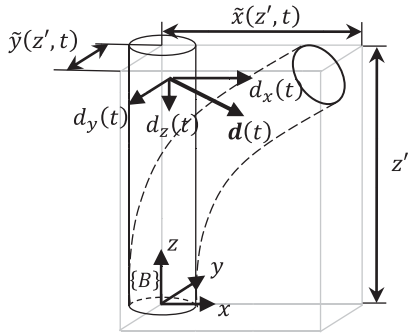

Fig. 3. Schematic of cantilever beam.

where function $\delta(z - z')$ is the Dirac delta function, defined as

$$\delta(z - z') = \begin{cases}\infty, & z = z' \\ 0, & \text{otherwise.}\end{cases} \tag{18}$$

Substituting (17) into the applied force in (15c) results in

$$\begin{aligned} f_{x,i} &= \int_0^L {}^Bp_x(t)\delta(z - z')\phi_i(z)dz \\ &= {}^Bp_x(t)\phi_i(z'), \qquad i = 1, \ldots, N. \end{aligned} \tag{19}$$

In vector form, it is expressed as

$$\boldsymbol{f}_x = \begin{bmatrix} f_{x,1} & \ldots & f_{x,N}\end{bmatrix}^T = {}^Bp_x(t)\boldsymbol{\phi}(z'). \tag{20}$$

Similarly, for y-direction

$$\boldsymbol{f}_y = {}^Bp_y(t)\boldsymbol{\phi}(z'). \tag{21}$$

The second-time derivatives of the coefficients $\ddot{\boldsymbol{\eta}}_x$ and in $\ddot{\boldsymbol{\eta}}_y$ can now be obtained separately by substituting the joint forces into (15) and the y-direction variant

$$\mathbf{M}_{b,y}\ddot{\boldsymbol{\eta}}_y + \mathbf{K}_{b,y}\boldsymbol{\eta}_y = \boldsymbol{f}_{b,y}. \tag{22}$$

The coefficients $\boldsymbol{\eta}_x$ and $\boldsymbol{\eta}_y$, hence, can be solved from the EoM of the beam (15) numerically, such as by the Runge–Kutta method. The deflection of any point on the beam can be computed by multiplying the coefficient to the corresponding comparison function by (8). Therefore, the total deflection can next be found by superposition method as shown in Fig. 3. In matrix form, the total deflection is

$$\begin{bmatrix}\tilde{x}(z',t)\\ \tilde{y}(z',t)\\ \tilde{z}(z',t)\end{bmatrix} = \begin{bmatrix}\boldsymbol{\phi}^T(z')\boldsymbol{\eta}_x(t)\\ \boldsymbol{\phi}^T(z')\boldsymbol{\eta}_y(t)\\ z'\end{bmatrix}. \tag{23}$$

The superposition principle is also applicable to multiple point forces on a single beam. Suppose the deflections of the beam due to the ith force is $[\tilde{x}_i\ \tilde{y}_i\ \tilde{z}_i]^T$ and there are m number of force acting on the beam, the total deflection would be

$$\begin{bmatrix}\tilde{x}(z',t)\\ \tilde{y}(z',t)\\ \tilde{z}(z',t)\end{bmatrix} = \sum_{i=1}^{m}\begin{bmatrix}\tilde{x}_i(z',t)\\ \tilde{y}_i(z',t)\\ \tilde{z}_i(z',t)\end{bmatrix} \tag{24}$$

which is the sum of deflection due to different forces as illustrated in Fig. 4. Hence, the above describes the procedures to

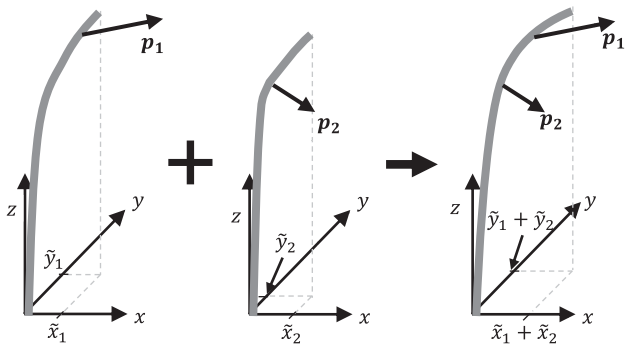

Fig. 4. Cantilever beam model with two point forces.

determine the single beam deflection when subject to arbitrary point forces (FD).

A *beam system* refers to multiple independent cantilever beams used as an open-frame structure for the D-CDPR. The equation of the beam system states is constructed by block diagonal matrices and block vectors which are from (15a) to (15c). The overall beam system could be represented by the following compact matrix form:

$$\mathbf{M}_b\ddot{\boldsymbol{\eta}} + \mathbf{C}_b\dot{\boldsymbol{\eta}} + \mathbf{K}_b\boldsymbol{\eta} = \boldsymbol{f}_b \tag{25}$$

where $\mathbf{M}_b$, $\mathbf{K}_b \in \mathbb{R}^{n_b \times n_b}$ are block diagonal matrices, with

$$\mathbf{M}_b = \begin{bmatrix} \mathbf{M}_{b_1,x} & \mathbf{0} & \cdots & \mathbf{0} & \mathbf{0} \\ \mathbf{0} & \mathbf{M}_{b_1,y} & \cdots & \mathbf{0} & \mathbf{0} \\ \vdots & \vdots & \ddots & \vdots & \vdots \\ \mathbf{0} & \mathbf{0} & \cdots & \mathbf{M}_{b_{m_b},x} & \mathbf{0} \\ \mathbf{0} & \mathbf{0} & \cdots & \mathbf{0} & \mathbf{M}_{b_{m_b},y} \end{bmatrix} \tag{25a}$$

$$\mathbf{K}_b = \begin{bmatrix} \mathbf{K}_{b_1,x} & \mathbf{0} & \cdots & \mathbf{0} & \mathbf{0} \\ \mathbf{0} & \mathbf{K}_{b_1,y} & \cdots & \mathbf{0} & \mathbf{0} \\ \vdots & \vdots & \ddots & \vdots & \vdots \\ \mathbf{0} & \mathbf{0} & \cdots & \mathbf{K}_{b_{m_b},x} & \mathbf{0} \\ \mathbf{0} & \mathbf{0} & \cdots & \mathbf{0} & \mathbf{K}_{b_{m_b},y} \end{bmatrix}. \tag{25b}$$

The vectors $\boldsymbol{\eta}$, $\boldsymbol{f}_b \in \mathbb{R}^{n_b}$ are the coefficients and applied force of the beams. They are block vectors that stores all joints and forces from independent beams

$$\boldsymbol{\eta}^T = \begin{bmatrix} \boldsymbol{\eta}_{b_1,x}^T & \boldsymbol{\eta}_{b_1,y}^T & \cdots & \boldsymbol{\eta}_{b_{m_b},x}^T & \boldsymbol{\eta}_{b_{m_b},y}^T \end{bmatrix} \tag{25c}$$

$$\boldsymbol{f}_b^T = \begin{bmatrix} \boldsymbol{f}_{b_1,x}^T & \boldsymbol{f}_{b_1,y}^T & \cdots & \boldsymbol{f}_{b_{m_b},x}^T & \boldsymbol{f}_{b_{m_b},y}^T \end{bmatrix}. \tag{25d}$$

The integer n_b is the total order of discretization (dimension of joint). It depends on the number of beams m_b, the dimension d of the Euclidean space that the beams lie on, and order of discretization of each beam n_j. Mathematically, it is

$$n_b = (d-1)\sum_{j}^{m_b} n_j. \tag{25e}$$

The term $\mathbf{C}_b = \alpha\mathbf{M}_b + \beta\mathbf{K}_b$ is the Rayleigh damping [34] with some constant α and β relating to the physical properties of the beam, which will be obtained from system identification experiments. Hence, (25) defines the EoM of the open-frame system and $\boldsymbol{f}_b$ is the external forces. Therefore, by employing the Galerkin method on EB beams, the frame could be expressed in a second-order ODE with the coefficient of the beam $\boldsymbol{\eta}$ as the state variable.

After introducing the kinematics and dynamics of the individual systems in Sections II and III-B, they can now be combined.

C. Kinematic Expression of the EB Beam System and CDPR

While the stationary exit points (those mounted at the fixture) still remain constant, the expression of moving exit points (those mounted on the deforming frame) is required. Suppose the ith exit point $\boldsymbol{a}_i$ is attached to the kth beam at $z = z_i$. As such, the exit point on the deflected beam ${}^{B_k}\boldsymbol{a}_i$ with respect to the beam frame $\{B_k\}$, can be found by (23), and hence

$${}^{B_k}\boldsymbol{a}_i = \begin{bmatrix} \boldsymbol{\phi}_k^T(z_i)\boldsymbol{\eta}_{k,x}(t) \\ \boldsymbol{\phi}_k^T(z_i)\boldsymbol{\eta}_{k,y}(t) \\ z_k \end{bmatrix}. \tag{26}$$

As such, the base exit point ${}^0\boldsymbol{a}_i$ in $\{0\}$ can be expressed as

$${}^0\boldsymbol{a}_i = {}^0_{B_k}\mathbf{R}\,{}^{B_k}\boldsymbol{a}_i + {}^0\boldsymbol{r}_k \tag{27}$$

where the ${}^0\boldsymbol{r}_k$ is the vector point to the origin of the beam k, as shown in Fig. 2. Note from (26) that the exit point and the beam's joint are linearly related.

Hence, the set of exit points on the D-CDPR can be represented in a block vector $\boldsymbol{a}_c = [{}^0\boldsymbol{a}_1{}^T \ldots {}^0\boldsymbol{a}_m{}^T]^T \in \mathbb{R}^{dm}$, where d is the dimension of Euclidean space that the robot lies on. The exit points can be expressed by

$$\boldsymbol{a}_c = \boldsymbol{\Phi}_a\boldsymbol{\eta} + \boldsymbol{y}_a \tag{28}$$

where $\boldsymbol{\Phi}_a \in \mathbb{R}^{dm \times n_b}$ is the mapping matrix, defined as

$$\boldsymbol{\Phi}_a = \begin{bmatrix} \boldsymbol{\Phi}_{a,11} & \cdots & \boldsymbol{\Phi}_{a,1k} & \cdots & \boldsymbol{\Phi}_{a,1m_b} \\ \vdots & \vdots & \vdots & \vdots & \vdots \\ \boldsymbol{\Phi}_{a,i1} & \cdots & \boldsymbol{\Phi}_{a,ik} & \cdots & \boldsymbol{\Phi}_{a,im_b} \\ \vdots & \vdots & \vdots & \vdots & \vdots \\ \boldsymbol{\Phi}_{a,m1} & \cdots & \boldsymbol{\Phi}_{a,mk} & \cdots & \boldsymbol{\Phi}_{a,mm_b} \end{bmatrix}. \tag{29}$$

Define an integer mapping function $g(i) = k$ that converts the exit point index i into beam index k. The submatrices $\boldsymbol{\Phi}_{a,ik}$ are defined as

$$\boldsymbol{\Phi}_{a,ik} = \begin{cases} {}^0_{g(i)}\mathbf{R}\boldsymbol{\Phi}_{bi} = {}^0_k\mathbf{R}\boldsymbol{\Phi}_{bi}, & \text{if } a_i \text{ on the beam } k \\ \mathbf{0}, & \text{otherwise.} \end{cases} \tag{30}$$

The rotation matrix ${}^0_{g(i)}\mathbf{R}$ rotates the point from $\{B_k\}$ to $\{0\}$. For the ith exit point on the kth beam

$$\boldsymbol{\Phi}_{bi} = \begin{cases} \begin{bmatrix} \boldsymbol{\phi}_{g(i)}^T(z_i) \\ \mathbf{0} \end{bmatrix} = \begin{bmatrix} \boldsymbol{\phi}_k^T(z_i) \\ \mathbf{0} \end{bmatrix}, & d = 2 \\ \begin{bmatrix} \boldsymbol{\phi}_{g(i)}^T(z_i) & \mathbf{0} \\ \mathbf{0} & \boldsymbol{\phi}_{g(i)}^T(z_i) \\ \mathbf{0} & \mathbf{0} \end{bmatrix} = \begin{bmatrix} \boldsymbol{\phi}_k^T(z_i) & \mathbf{0} \\ \mathbf{0} & \boldsymbol{\phi}_k^T(z_i) \\ \mathbf{0} & \mathbf{0} \end{bmatrix}, & d = 3. \end{cases} \tag{31}$$

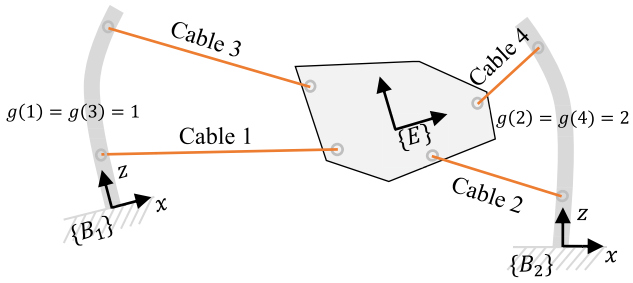

Fig. 5. Example D-CDPR to show the relationship between beams' coefficients to exit points.

The vector $\boldsymbol{y}_a \in \mathbb{R}^{dm}$ is the offset vector, constructed as

$$\boldsymbol{y}_a = \mathbf{R}_b \begin{bmatrix} [0 \quad 0 \quad z_1]^T \\ \vdots \\ [0 \quad 0 \quad z_m]^T \end{bmatrix} + \begin{bmatrix} {}^0_{g(1)}\boldsymbol{r} \\ \vdots \\ {}^0_{g(m)}\boldsymbol{r} \end{bmatrix}. \tag{32}$$

With (28), a relation to transform the beam coefficients into exit points on the frame is established. Below is an example mapping matrix of the D-CDPR shown in Fig. 5

$$\boldsymbol{\Phi}_a = \begin{bmatrix} {}^0_{B_1}\mathbf{R}\boldsymbol{\Phi}_{b1} & \mathbf{0} \\ \mathbf{0} & {}^0_{B_2}\mathbf{R}\boldsymbol{\Phi}_{b2} \\ {}^0_{B_1}\mathbf{R}\boldsymbol{\Phi}_{b3} & \mathbf{0} \\ \mathbf{0} & {}^0_{B_2}\mathbf{R}\boldsymbol{\Phi}_{b4} \end{bmatrix} \in \mathbb{R}^{8\times n_b}. \tag{33}$$

Because the first and third exit points are on the first beam B_1, $g(1) = g(3) = 1$ and the first column of $\boldsymbol{\Phi}_a$ in (33) is nonzero on the first and third rows. The second column, which represents the second beam, on the other hand, has a nonzero second and forth rows that represents the second and the forth exit points.

D. Dynamic Expression of the EB Beam System and CDPR

For the force relation, the cable tension $\boldsymbol{\tau}$ deforms the beams in addition to providing a wrench to the EE. The cable forces (cable tension with directions) can be modeled as a series of external point forces acting on the beams. The force vector w.r.t. $\{0\}$ of the ith cable, ${}^0\boldsymbol{f}_i$ can be obtained by

$${}^0\boldsymbol{f}_i = {}^0\hat{\boldsymbol{c}}_i\, \tau_i. \tag{34}$$

Again, suppose the ith cable tension τ_i is applied to the kth beam at $z = z_k$. By (20) and (21), the beam joint forces in x and y directions are

$$\boldsymbol{f}_k = \begin{bmatrix} \boldsymbol{f}_{k,x} \\ \boldsymbol{f}_{k,y} \end{bmatrix} = \begin{bmatrix} \phi_k(z_k) & \mathbf{0} & \mathbf{0} \\ \mathbf{0} & \phi_k(z_k) & \mathbf{0} \end{bmatrix} {}^{B_k}_0\mathbf{R}\, {}^0\hat{\boldsymbol{c}}_i\, \tau_i. \tag{35}$$

Defining a cable force vector $\boldsymbol{\tau}_c \in \mathbb{R}^{dm}$ that contains all cable forces

$$\boldsymbol{\tau}_c = \begin{bmatrix} {}^0\hat{\boldsymbol{c}}_1\tau_1 \\ \vdots \\ {}^0\hat{\boldsymbol{c}}_m\tau_m \end{bmatrix} = \begin{bmatrix} {}^0\hat{\boldsymbol{c}}_1 & \cdots & \mathbf{0} \\ \vdots & \ddots & \vdots \\ \mathbf{0} & \cdots & {}^0\hat{\boldsymbol{c}}_m \end{bmatrix} \boldsymbol{\tau} := \mathbf{L}\boldsymbol{\tau}. \tag{36}$$

Finally, by taking into account all cable tension and beam joint force, the relationship between $\boldsymbol{\tau}_c$ and $\boldsymbol{f}_b$ can be expressed using the $\boldsymbol{\Phi}_a$ as derived in (28), where

$$\boldsymbol{f}_b = \boldsymbol{\Phi}_a^T \boldsymbol{\tau}_c = \boldsymbol{\Phi}_a^T \mathbf{L}\boldsymbol{\tau}. \tag{37}$$

E. EoM of a D-CDOR With EB Beams

The cable tension τ would cause certain wrenches onto the EE and the beam. By combining (25) and (2), the EoM of the entire D-CDPR can now be expressed as

$$\begin{cases} \mathbf{M}(\boldsymbol{q})\ddot{\boldsymbol{q}} + \mathbf{C}(\dot{\boldsymbol{q}}, \boldsymbol{q}) + \boldsymbol{g}(\boldsymbol{q}) = \mathbf{W}(\boldsymbol{q}, \boldsymbol{\eta})\boldsymbol{\tau} \\ \mathbf{M}_b\ddot{\boldsymbol{\eta}} + \mathbf{C}_b\dot{\boldsymbol{\eta}} + \mathbf{K}_b\boldsymbol{\eta} = \boldsymbol{f}_b = \mathbf{W}_b(\boldsymbol{q}, \boldsymbol{\eta})\boldsymbol{\tau} \end{cases} \tag{38}$$

where $\mathbf{W}_b = \boldsymbol{\Phi}_a^T\mathbf{L}$. With the expressions, the EoM in (5) could be crafted into a more specific form (38).

IV. D-CDPR Forward and ID

The FD and the ID of the D-CDPR will be discussed in this section. The FD is used in the simulation to better understand the D-CDPR's behavior. The ID, on the other hand, governs the cable tension command for the EE's desired motion.

A. Forward Dynamics

From the dynamics model of the D-CDPR (38), the overall dynamics could be combined as a time-variant nonlinear system. At each time step, the wrench matrix $\mathbf{W}$ of the CDPR and the mapping matrix $\mathbf{W}_b$ of the frame can be determined by knowing or measuring the state of the CDPR $\boldsymbol{q}$ and the state of the beam $\boldsymbol{\eta}$. The output state $\boldsymbol{y_s}$ of the overall system is $\boldsymbol{q}$. Hence, the state-space equation of the overall system is

$$\begin{aligned} \dot{\boldsymbol{x}}_s &= \mathbf{A}_s\boldsymbol{x}_s + \mathbf{B}_s\boldsymbol{u}_s \\ \boldsymbol{y}_s &= \mathbf{C}_s\boldsymbol{x}_s \end{aligned} \tag{39}$$

or in the expanded form

$$\dot{\boldsymbol{x}}_s = \begin{bmatrix} \mathbf{0} & \boldsymbol{I} & \mathbf{0} & \mathbf{0} \\ \mathbf{0} & \mathbf{0} & \mathbf{0} & \mathbf{0} \\ \mathbf{0} & \mathbf{0} & \mathbf{0} & \boldsymbol{I} \\ \mathbf{0} & \mathbf{0} & -\mathbf{M}_b^{-1}\mathbf{K} & -\mathbf{M}_b^{-1}\mathbf{C}_b \end{bmatrix} \begin{bmatrix} \boldsymbol{q} \\ \dot{\boldsymbol{q}} \\ \boldsymbol{\eta} \\ \dot{\boldsymbol{\eta}} \end{bmatrix} + \begin{bmatrix} \mathbf{0} & \mathbf{0} \\ \mathbf{M}^{-1}\mathbf{W} & -\mathbf{M}^{-1} \\ \mathbf{0} & \mathbf{0} \\ \mathbf{M}_b^{-1}\mathbf{W}_b & \mathbf{0} \end{bmatrix} \begin{bmatrix} \boldsymbol{\tau} \\ \mathbf{C} + \boldsymbol{g} + \boldsymbol{w}_{\text{ext}} \end{bmatrix}$$

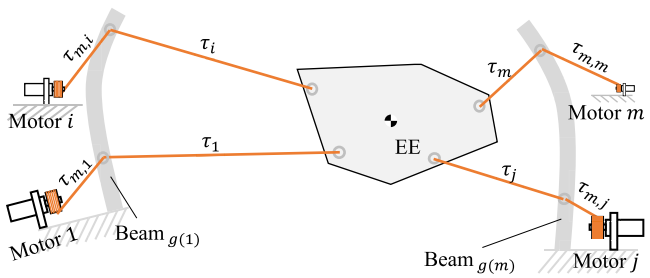

Fig. 6. Cable tension and actuators for the D-CDPR system.

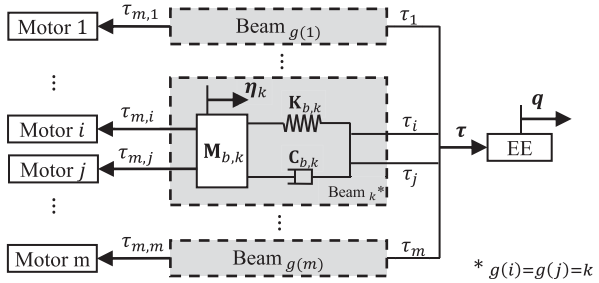

Fig. 7. Model of the motor tension to the EE.

$$\boldsymbol{y}_s = \begin{bmatrix} \boldsymbol{I} & \mathbf{0} & \mathbf{0} & \mathbf{0} \end{bmatrix} \begin{bmatrix} \boldsymbol{q} \\ \dot{\boldsymbol{q}} \\ \boldsymbol{\eta} \\ \dot{\boldsymbol{\eta}} \end{bmatrix}. \tag{40}$$

The output $\boldsymbol{q}$ is the CDPR EE pose and will be used to evaluate the tracking performance of the system.

In this work, a discretized state-space EoM with fixed time step will be used, to lower the computational effort and to be more convenient for execution on D-CDPR. Letting $\boldsymbol{x}[k]$, $\boldsymbol{u}[k]$, $\boldsymbol{y}[k]$ be the state, input, and output at the kth time step, respectively, with Δ_t as the time step. At $t = k+1$

$$\begin{aligned} \boldsymbol{x}[k+1] &= \mathbf{A}_d \boldsymbol{x}[k] + \mathbf{B}_d \boldsymbol{u}[k] \\ \boldsymbol{y}[k] &= \mathbf{C}_d \boldsymbol{x}[k] \end{aligned} \tag{41}$$

where

$$\begin{aligned} \mathbf{A}_d &= e^{\mathbf{A}_s \Delta_t} \\ \mathbf{B}_d &= \int_{k\Delta_t}^{(k+1)\Delta_t} e^{\mathbf{A}_s((k+1)\Delta_t - \tau)} d\tau \mathbf{B}_s \\ \mathbf{C}_d &= \mathbf{C}_s. \end{aligned}$$

With the FD (41), the behavior of both the frame and the EE could then be determined.

B. Inverse Dynamics

ID refers to determination of the required cable tension $\boldsymbol{\tau}$ for the desired task motion $\tilde{\boldsymbol{q}}$, velocity $\dot{\tilde{\boldsymbol{q}}}$, and acceleration $\ddot{\tilde{\boldsymbol{q}}}$. Note that for a redundantly actuated CDPR, there exists multiple combinations of cable tension that generate the same desired acceleration. Moreover, the nonlinearity of the wrench matrix and positive cable tension constraint create challenges in solving the ID.

Fig. 6 shows an overview of cable linkage from the motors to the EE. Fig. 7 shows the free body diagram of a general type D-CDPR. The cables that are connecting the EE provide tension $\boldsymbol{\tau}$, which provide wrenches on to the EE to produce the desired acceleration. When calculating the required command tension $\boldsymbol{\tau}_m$ for the motors, the EoM of D-CDPR systems must be taken into account.

In this work, an optimization-based approach is proposed to solve the ID, by considering the positive force constraint and coupled EoM including the dynamics of the deforming frame into the solver. This also allows additional objectives to be fulfilled by using the null space of the cable tension redundancy. The EoM with the desired acceleration command can be formulated either as a soft or a hard constraint. For hardware implementation, treating the EoM as a soft constraint is preferred for situations where the solver may fail to find a feasible cable tension solution due to demanding tracking gains or large tracking error [35]. As such, the following ID problem is proposed:

$$\begin{aligned} \underset{\boldsymbol{\tau}_m}{\text{argmin}} \quad & b\|\mathbf{W}\boldsymbol{\tau} - \tilde{\boldsymbol{w}}\|_2^2 + \boldsymbol{h}_o(\boldsymbol{\tau}_m) \\ \text{s.t.} \quad & \mathbf{W}_b \boldsymbol{\tau}_m = \mathbf{M}_b \ddot{\boldsymbol{\eta}} + \mathbf{C}_b + \mathbf{K}_b - \boldsymbol{\tau} \\ & \mathbf{0} \le \boldsymbol{\tau}_m \le \overline{\boldsymbol{\tau}}_m \\ & \underline{\boldsymbol{\tau}} \le \boldsymbol{\tau} \le \overline{\boldsymbol{\tau}} \end{aligned} \tag{42}$$

where

$$\tilde{\boldsymbol{w}} = \mathbf{M}\ddot{\tilde{\boldsymbol{q}}} + \mathbf{C} + \boldsymbol{g} + \boldsymbol{w}_{\text{ext}}. \tag{43}$$

The term $\boldsymbol{h}_o(\boldsymbol{\tau}_m)$ is the extra objective function dependent on $\boldsymbol{\tau}_m$. The scalar b controls the weighting of tracking performance over other objectives, where usually $b \gg 1$ to prioritize the tracking performance. Here, $\ddot{\tilde{\boldsymbol{q}}} = [\ddot{\tilde{\boldsymbol{q}}}_p, \ddot{\tilde{\boldsymbol{q}}}_r]$ is the command acceleration that consists of both translational and rotational acceleration, which will be defined in Section VI.

In the following, two objective functions are proposed for the D-CDPR ID. The first is to minimize the cable tensions for the D-CDPR, which reduces the beam deflection and possible inaccuracies caused by large deflections. Setting $\boldsymbol{h}_o(\boldsymbol{\tau}_m)$ as the second norm of the cable tension vector, the extra objective function becomes

$$\boldsymbol{h}_o(\boldsymbol{\tau}_m) = \|\boldsymbol{\tau}_m\|_2^2. \tag{44}$$

Due to the fact that the dynamics properties of the beam are less accurate and hard to measure, it is desirable to lower the dynamic effect of the beam in order to reduce the modeling error. To prevent rapid changing cable tension from exciting high dynamic effect. The objective function

$$\boldsymbol{h}_o(\boldsymbol{\tau}_m) = \|\boldsymbol{\tau}_m - \boldsymbol{\tau}'_m\|_2^2 \tag{45}$$

where $\boldsymbol{\tau}'_m$ is the previous cable tension command, aims at minimizing the change of cable tension. Note that the choice

of extra objective functions (44) and (45) allow the optimization problem to be solved by quadratic programming.

V. Workspace Analysis of D-CDPR

The analysis of the workspace is essential to gain an understanding of the region that the EE could physically reach. In this article, the AWS is analyzed first to showcase the differences between the conventional CDPR's and D-CDPR's AWS. This analysis helps to explain the unusual SW of the D-CDPR, which is discussed in the second part of this section. Next, the static conditions of the D-CDPR are formulated, and the SW is compared with the conventional CDPR's SW.

A. AWS of the D-CDPR

The AWS is the set of EE wrenches that can be produced by the available cable tension combinations. Mathematically, the AWS of a rigid frame CDPR is

$$\mathrm{AWS_r}(\boldsymbol{q_c}) = \{\boldsymbol{w} \in \mathbb{R}^n : \boldsymbol{w} = \mathbf{W}(\boldsymbol{q})\boldsymbol{\tau} \quad \forall \boldsymbol{\tau} \in [\underline{\boldsymbol{\tau}}, \overline{\boldsymbol{\tau}}]\}. \quad (46)$$

For rigid frame CDPRs, whose base frame exit points' locations $\boldsymbol{a}$ are constant, the wrench matrix $\mathbf{W}$ is also constant for a given pose $\boldsymbol{q}$. By expanding the equation in (46), any wrench $\boldsymbol{w}$ generated by feasible cable tension could be represented by

$$\boldsymbol{w} = \sum_{i=1}^{m} \tau_i \hat{\boldsymbol{w}}_i \quad (47)$$

where $\hat{\boldsymbol{w}}_i$ is the ith column of the wrench matrix, or the unit wrench vector of the ith cable.

According to [33], the AWS of a rigid frame CDPR (AWS_r) at a fixed pose is a convex zonotope, whose bounding hyperplanes is spanned by combinations of cable tension. They can also be parameterized by the cable tension $\boldsymbol{\tau}$. The kth hyperplane consists of the following three subsets of cable tensions:

1) those that shift the plane, i.e., $\forall \overline{\tau}_i \hat{\boldsymbol{w}}_i,\ i \in \mathcal{Z}_k$;
2) those that span the plane, i.e., $\forall \tau_j \hat{\boldsymbol{w}}_j,\ j \in \mathcal{Y}_k$;
3) those that are the remaining, i.e., $\forall \underline{\tau}_i \hat{\boldsymbol{w}}_i,\ i \notin \mathcal{Z}_k \cup \mathcal{Y}_k$.

Let $\mathcal{Z}_k$ be an integer set that stores the indices of the cable tensions those that shift the kth plane. Let $\mathcal{Y}_k$ be another integer set that stores the indices of the cable tension that span the kth plane whose parametric equation in the wrench space is

$$\boldsymbol{w}_k(\boldsymbol{\tau}) = \sum_{j \in \mathcal{Y}_k} \tau_j \hat{\boldsymbol{w}}_j + \sum_{i \in \mathcal{Z}_k} \overline{\tau}_i \hat{\boldsymbol{w}}_i + \sum_{\substack{i \notin \mathcal{Y}_k \\ i \notin \mathcal{Z}_k}} \underline{\tau}_i \hat{\boldsymbol{w}}_i \quad (48)$$

where $\tau_j \in [\underline{\tau}_j, \overline{\tau}_j]$. In other words, the plane spanned by the $\mathcal{Y}_k$th cable forces is shifted by the wrenches generated by cable forces in $\mathcal{Z}_k$. Noted that different planes are contributed by different combinations of $\mathcal{Y}_k$ and $\mathcal{Z}_k$.

An AWS example of a 3-cable 2-DoF rigid frame CDPR is shown in Fig. 8. The first plane is spanned by the third cable vector, hence $\mathcal{Y}_1 = \{3\}$. It is shifted by wrench $\overline{\tau}_2\, {}^0\hat{\boldsymbol{w}}_2$, hence, $\mathcal{Z}_1 = \{2\}$. The parametric equations are shown in the figure.

For D-CDPRs, the unit wrench vector $\hat{\boldsymbol{w}}$ is a function of the exit points, which depend on cable tension and cable vector. Consider that in quasi-static state, the exit points could be

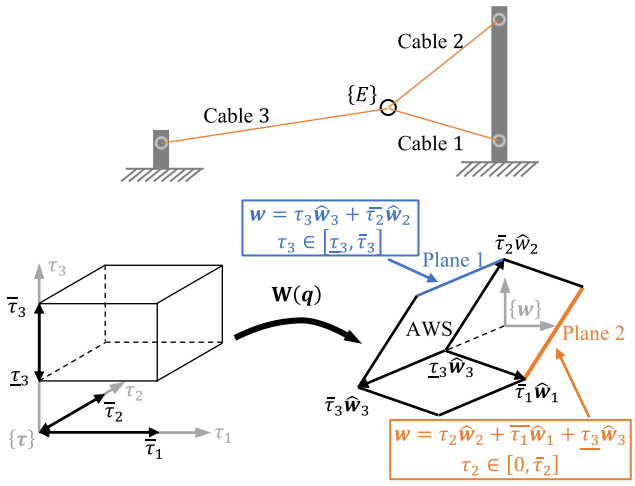

Fig. 8. AWS example of a rigid frame CDPR. The parametric equations of two of the boundaries are written out.

expressed by combining the second and third constraints from (52)

$$\boldsymbol{a} = \boldsymbol{\Phi}_a \mathbf{K}_b^{-1} \mathbf{W}_b(\boldsymbol{q}, \boldsymbol{\eta})\, \boldsymbol{\tau} + \boldsymbol{y}_a. \quad (49)$$

It should be noted that the change in cable tension magnitude affects the supporting beams' deflection and hence the direction of the cable force acting on the EE. Hence, the kth bounding planes of the AWS of D-CDPRs could be found by the following procedures.

1) Discretize τ_j into a finite number of steps for one member from $j \in \mathcal{Y}_k$.
2) For each step, construct the tension vector as $\boldsymbol{\tau} = \underline{\boldsymbol{\tau}}$ except for the jth element and ith elements, where $i \in \mathcal{Z}_k$ and $j \in \mathcal{Y}_k$.
3) For the jth element, τ_j is set to the discretized cable tension as defined in step (1). For the ith elements, $\tau_i = \overline{\tau}_i$.
4) Obtain $\boldsymbol{a}$ by substituting $\boldsymbol{\tau}$ into (49).
5) One step of the bounding plane $\boldsymbol{w}_k$ could be obtain numerically by substituting $\boldsymbol{a}$, τ_j, $\overline{\tau}_i$, $\underline{\tau}_i$ into (48).
6) Repeat the abovementioned process (1)–(5) until all corresponding $\boldsymbol{w}_k$ of all steps and all j are calculated. The bounding plane is obtained.

The orange plane ($k = 2$) in Fig. 8 would be selected as an example. From the figure, $\tau_2\hat{\boldsymbol{w}}_2$ is the parameter and it spans the plane, thus, $\mathcal{Y}_2 = \{2\}$. Cable 1 shift the plane, thus, $\mathcal{Z}_2 = \{1\}$.

1) Suppose τ_2 is discretized into 10 steps $\tau_s \in [\underline{\tau_2}, \overline{\tau_2}]$, $\forall \tau_s = 1, \ldots, 10$.
2) Set $\boldsymbol{\tau} = [*, *, \underline{\tau_3}]^T$ as $i = 1$ and $j = 2$.
3) Set the first element and the second element of $\boldsymbol{\tau}$ as $\overline{\tau_1}$ and τ_s, respectively, such that $\boldsymbol{\tau} = [\overline{\tau_1}, \tau_s, \underline{\tau_3}]^T$ is a constant.
4) Substitute $\boldsymbol{\tau}$ into (49) to obtain the the exit points $\boldsymbol{a}$ under this combination of cable tension.
5) The cable tension can be mapped into wrench space by (48).
6) Repeat the steps 1)–5) 10 times until all combinations of the disrectized τ_2 is converted into wrench space.

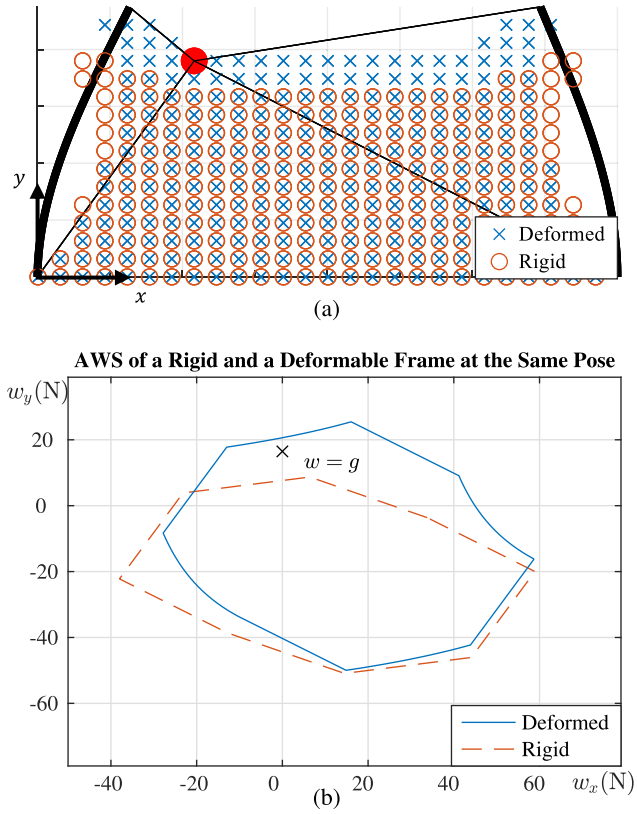

Fig. 9. (a) SWs of a planar CDPR with rigid or deformable frame. (b) AWSs of the robot at a particular pose.

With these procedures, the AWS for D-CDPR could be obtained. Consider a redundantly actuated planar D-CDPR as shown in Fig. 9(a) (of which the SW is also plotted), the AWS of this robot at the same pose is shown in Fig. 9(b). The exit points move toward the cable force direction thus the hyperplanes tend to curve along with the bending direction.

B. Static Workspace

SW is defined as the set of poses where the EE could sustain its own weight (static condition or SC). The equilibrium equation could be interpreted as a special case of the D-CDPR's EoM (38), where $\ddot{\boldsymbol{q}} = \dot{\boldsymbol{q}} = \ddot{\boldsymbol{\eta}} = \dot{\boldsymbol{\eta}} = \mathbf{0}$ and hence

$$\begin{aligned} \boldsymbol{g}(\boldsymbol{q}) &= \mathbf{W}(\boldsymbol{q}, \boldsymbol{\eta})\boldsymbol{\tau} \\ \mathbf{K}_b\boldsymbol{\eta} &= \mathbf{W}_b(\boldsymbol{q}, \boldsymbol{\eta})\,\boldsymbol{\tau}. \end{aligned} \tag{50}$$

A given pose fulfills the SC, if and only if there exists an available cable tension that could satisfy the equilibrium equation (50). Mathematically, it is defined as

$$\mathrm{SW} = \left\{ \boldsymbol{q} \;\middle|\; \begin{matrix} \boldsymbol{g}(\boldsymbol{q}) = \mathbf{W}(\boldsymbol{q}, \boldsymbol{\eta})\boldsymbol{\tau} \\ \mathbf{K}_b\boldsymbol{\eta} = \mathbf{W}_b(\boldsymbol{q}, \boldsymbol{\eta})\,\boldsymbol{\tau} \end{matrix} \;,\; \exists \boldsymbol{\tau} \in [\underline{\boldsymbol{\tau}}, \overline{\boldsymbol{\tau}}] \right\}. \tag{51}$$

Due to the nonlinearity of the wrench matrix $\mathbf{W}$ with respect to $\boldsymbol{\eta}$, nonlinear programming (NLP) is used to evaluate the SC.

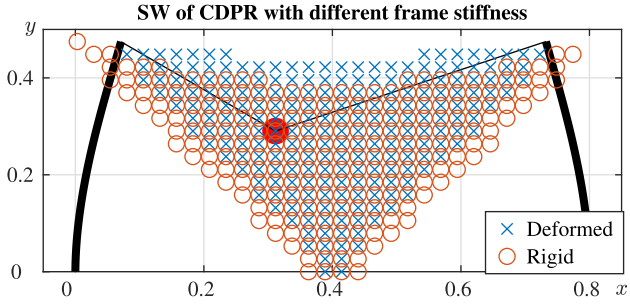

Fig. 10. SW of a planar rigid CDPR and D-CDPR.

If the pose satisfies the SC, then there exists a solution $\boldsymbol{\tau}$ to

$$\begin{aligned} \min_{\boldsymbol{\tau},\boldsymbol{\eta}} \quad & \|\boldsymbol{\tau}\|_2 \\ \text{s.t.} \quad & \boldsymbol{g}(\boldsymbol{q}) = \mathbf{W}(\boldsymbol{q}, \boldsymbol{a}(\boldsymbol{\eta}))\boldsymbol{\tau} \\ & \boldsymbol{a} = \boldsymbol{\Phi}_a\boldsymbol{\eta} + \boldsymbol{y}_a \\ & \boldsymbol{\eta} = \mathbf{K}_b^{-1}\mathbf{W}_b(\boldsymbol{q}, \boldsymbol{\eta})\,\boldsymbol{\tau} \\ & \underline{\boldsymbol{\tau}} \le \boldsymbol{\tau} \le \overline{\boldsymbol{\tau}}. \end{aligned} \tag{52}$$

In this work, the interior point algorithm [36], implemented by `fmincon` in MATLAB was used, to solve this constrained nonlinear multivariable optimization problem (52). The SW of the first D-CDPR example as shown in Fig. 10 is a 2-beam and 2-cable point mass D-CDPR with 2 DoFs EE. The SW of a rigid frame CDPR with the same exit point location is also evaluated and plotted in Fig. 10.

It demonstrates that the D-CDPR SW has greater coverage on the top side but less on the two sides. This phenomenon is analyzed and expressed with the aid of the wrench set concept for D-CDPR in the previous Section V-A. Referring to the Fig. 9, the AWS_d is deformed to become taller and thinner compared to the AWS_r. As a result, $\boldsymbol{g} \in \mathrm{AWS}_d$ but $\boldsymbol{g} \notin \mathrm{AWS}_r$. Hence, the EE is at a point where the rigid frame CDPR is out of SW whilst the D-CDPR is within the workspace.

A second D-CDPR example is a 4-beam, 8-cable, and 3-DoF point mass D-CDPR, as shown in Fig. 11(a). In this example, the beams are significantly stiffer (in the magnitude of 10^2) along yz plane than xz plane. They could be considered as thin plates. As can be seen from Fig. 11(b) and (c), similar trend of reshaped workspace is found for these 3-D CDPRs.

It is worth noting that the NLP method is conservative (a feasible solution might not be found) since the solver might converge to a locally infeasible point. To increase the successful search rate and decrease the evaluation time, it is proposed to set the initial guess of each NLP (52) as the nearest feasible point (NFP). This method relies on the observation that the difference between the optimal solutions of two adjacent workspace points is small. The upper left plot of Fig. 12 shows that using random initial guess, the NLP solver misses several SW points as it fails to converge to any feasible solution. Moreover, Table I shows the computational time required for generating the workspace of different D-CDPRs. The computational time is around 10% faster when using NFP initial guess than when using random

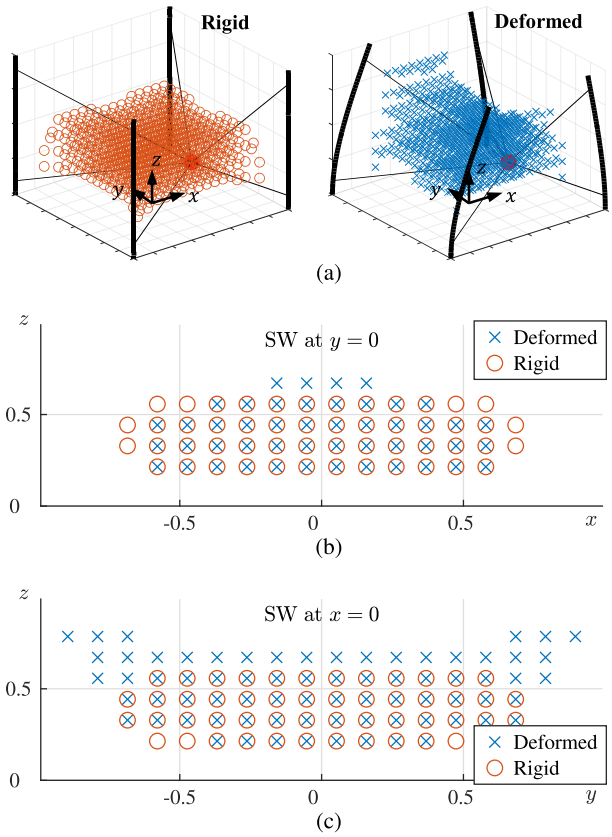

Fig. 11. (a) SW of a spatial rigid CDPR (left) and D-CDPR (right). (b) Cross-sectional view of SW of a spatial rigid CDPR and D-CDPR for $y = 0$. (c) Cross-sectional view of SW of a spatial rigid CDPR and D-CDPR for $x = 0$.

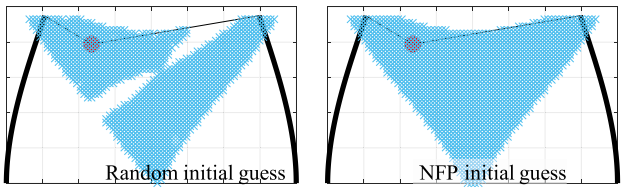

Fig. 12. Comparison using different initial conditions to the NLP.

TABLE I
COMPARISON OF COMPUTATIONAL TIME OF DIFFERENT D-CDPR

D-CDPR type	Computational time (s) NFP	Random	m	n	No. of points
Point mass planar	102	130	2	2	3696
Point mass planar	213	233	3	2	3696
Point mass spatial	$3.04(10^3)$	$3.42(10^3)$	8	3	3200
6-DoF spatial	$4.62(10^4)$	$5.25(10^4)$	8	6	38 400

guess, which makes a significant difference when calculating workspaces with a high DoF or a large number of points.

VI. D-CDPR CONTROL STRATEGY

This section presents a novel control scheme suitable for D-CDPRs. The controller consists of two components: 1) tension control; and 2) MBFL control.

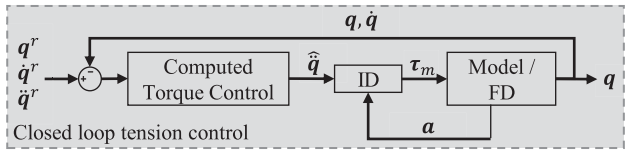

Fig. 13. Block diagram of closed-loop tension control D-CDPR.

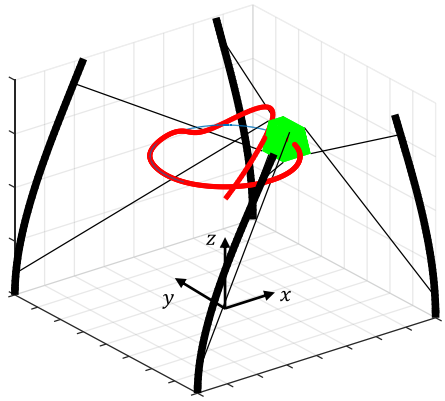

Fig. 14. 4-beam, 8-cable D-CDPR with a trapezoidal prism EE. The circle-shaped reference trajectory. On top of the reference trajectory, the motion history is shown as a red line on the graph.

A. Tension Control

In this work, the command acceleration is produced by the common computed-torque control law, where the command translational acceleration is

$$\hat{\ddot{\boldsymbol{q}}}_p = \ddot{\boldsymbol{q}}_p^r + k_{d,p}(\dot{\boldsymbol{q}}_p^r - \dot{\boldsymbol{q}}_p) + k_{p,p}(\boldsymbol{q}_p^r - \boldsymbol{q}_p) \tag{53}$$

and the command rotational acceleration is

$$\hat{\ddot{\boldsymbol{q}}}_r = \ddot{\boldsymbol{q}}_r^r + k_{d,r}(\dot{\boldsymbol{q}}_r^r - \dot{\boldsymbol{q}}_r) + k_{p,r} RV({}^{E^r}_{E}\mathbf{R}) \tag{54}$$

where $\boldsymbol{q}^r = [\boldsymbol{q}_p^{rT}, \boldsymbol{q}_r^{rT}]^T$ is the reference pose. The function RV: $\mathrm{SO}(3) \to \mathbb{R}^3$ converts the rotation matrix to a rotation vector [37]. The rotation matrix ${}^{E^r}_{E}\mathbf{R}$ rotates the points in actual EE frame $\{E\}$ to the reference EE frame $\{E^r\}$. The positive scalars $k_{p,p}, k_{d,p}, k_{p,r}, k_{d,r}$ are the position and velocity gains. The command acceleration would be converted into command cable tension by the ID (42) using the proposed D-CDPR model from Sections III and IV. Fig. 13 shows the block diagram of the tension control.

A 6-DoF ($n = 6$), 8-cable ($m = 8$), 4 beams D-CDPR that lies in the 3-D space ($d = 3$) was tracking a circular trajectory in the simulation. The undeformed frame has a size of $2 \times 2 \times 1\mathrm{m}^3$ and the setup is shown in Fig. 14. The EE is a trapezoidal prism with a dimension approximately equal to $0.2 \times 0.2 \times 0.1\,\mathrm{m}^3$. The inertial frame origin is located at the bottom center of the workspace. The beams have different bending properties at x and y axes such that they could be treated as spring-steel plates. The details of the exit points and the beams are listed in Tables II and III, respectively.

TABLE II
EXIT POINTS OF THE 6-DOF D-CDPR

i	1	2	3	4	5	6	7	8
${}^0\boldsymbol{a}_i$ (m)	$\begin{bmatrix}1.0\\-1.0\\0.1\end{bmatrix}$	$\begin{bmatrix}1.0\\-1.0\\0.9\end{bmatrix}$	$\begin{bmatrix}1.0\\1.0\\0.1\end{bmatrix}$	$\begin{bmatrix}1.0\\1.0\\0.9\end{bmatrix}$	$\begin{bmatrix}-1.0\\1.0\\0.1\end{bmatrix}$	$\begin{bmatrix}-1.0\\1.0\\0.9\end{bmatrix}$	$\begin{bmatrix}-1.0\\-1.0\\0.1\end{bmatrix}$	$\begin{bmatrix}-1.0\\-1.0\\0.9\end{bmatrix}$
${}^E\boldsymbol{b}_i$ (cm)	$\begin{bmatrix}6.2\\-11.5\\6.6\end{bmatrix}$	$\begin{bmatrix}11.5\\-11.5\\-6.6\end{bmatrix}$	$\begin{bmatrix}6.2\\11.5\\6.6\end{bmatrix}$	$\begin{bmatrix}11.5\\11.5\\-6.6\end{bmatrix}$	$\begin{bmatrix}-6.2\\11.5\\6.6\end{bmatrix}$	$\begin{bmatrix}-11.5\\11.5\\-6.6\end{bmatrix}$	$\begin{bmatrix}-6.2\\-11.5\\6.6\end{bmatrix}$	$\begin{bmatrix}-11.5\\-11.5\\-6.6\end{bmatrix}$

TABLE III
BEAM PROPERTIES OF THE 6-DOF D-CDPR

k	1	2	3	4
$\mathrm{EI}_{x,k}$ (N·m^2)	7.81			
$\mathrm{EI}_{y,k}$ (10^3 N·m^2)	1.13			
ρA (k·g·m^{-1})	0.589			
${}^0_{B_k}\mathbf{R}$	$\boldsymbol{I}_3$			
${}^0_k\boldsymbol{r}$ (m)	$\begin{bmatrix}1.0\\1.0\\0.0\end{bmatrix}$	$\begin{bmatrix}1.0\\1.0\\0.0\end{bmatrix}$	$\begin{bmatrix}1.0\\1.0\\0.0\end{bmatrix}$	$\begin{bmatrix}1.0\\1.0\\0.0\end{bmatrix}$

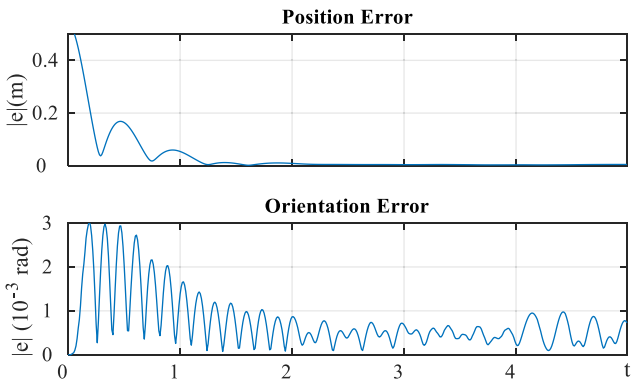

Fig. 15. Position and orientation error of the EE tracking the circular trajectory from Fig. 14.

All cables have a force limit of $0 \leq \tau \leq 80$ N. The initial state of the EE is

$$\boldsymbol{q}_0 = \begin{bmatrix}0 & 0 & \frac{1}{2} & 0 & 0 & 0\end{bmatrix}^T$$
$$\dot{\boldsymbol{q}}_0 = \ddot{\boldsymbol{q}}_0 = \boldsymbol{0}. \tag{55}$$

The first reference trajectory is

$$\boldsymbol{q}^r = \frac{1}{2}\begin{bmatrix}\cos(\gamma t) & \sin(\gamma t) & 1.4 & 0 & 0 & 0\end{bmatrix}^T$$
$$\dot{\boldsymbol{q}}^r = \frac{1}{2}\begin{bmatrix}-\gamma\sin(\gamma t) & \gamma\cos(\gamma t) & 0 & 0 & 0 & 0\end{bmatrix}^T$$
$$\ddot{\boldsymbol{q}}^r = -\frac{1}{2}\begin{bmatrix}\gamma^2\cos(\gamma t) & \gamma^2\sin(\gamma t) & 0 & 0 & 0 & 0\end{bmatrix}^T \tag{56}$$

where $\gamma = 0.4\pi$. The simulation ran at a discrete-time frequency of 100 Hz. The EE started at the center of the workspace, hence, it had a very large position error initially. However, the position and orientation errors converged to $\|\boldsymbol{e}_p\| < 3$ mm $\|\boldsymbol{e}_r\| = \|\boldsymbol{q}_r - \boldsymbol{q}_r^r\| < 10^{-3}$ rad, respectively, for $t > 2$ s. The error plots are displayed in Fig. 15.

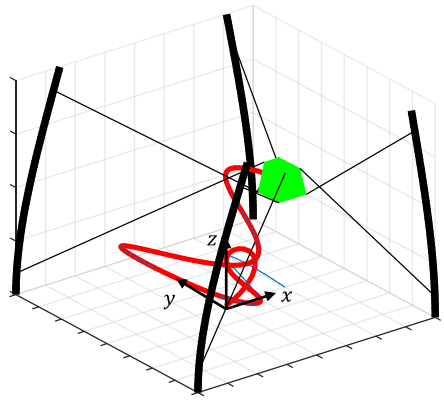

Fig. 16. Component functions of the second reference trajectory are sinusoidal.

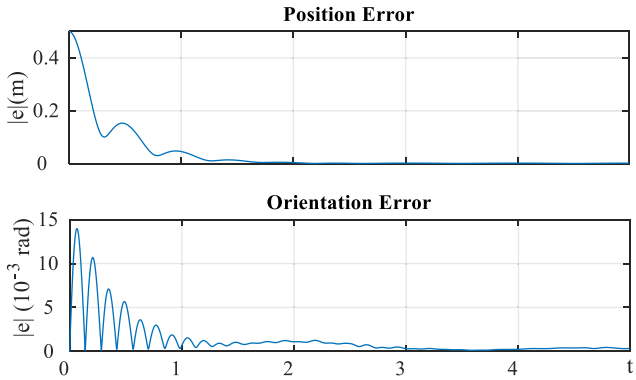

Fig. 17. Position and orientation error of the EE tracking the sinusoidal trajectory from Fig. 16.

The second reference trajectory (shown in Fig. 16) included rotation, given by

$$\boldsymbol{q}^r = \begin{bmatrix}\frac{1}{2}\cos(\gamma_1 t) & \frac{1}{2}\sin(\gamma_2 t) & \frac{1}{10}t & \frac{1}{3}\sin(\gamma_1 t) & 0 & 0\end{bmatrix}^T$$
$$\dot{\boldsymbol{q}}^r = \begin{bmatrix}\frac{-\gamma_1}{2}\sin(\gamma_1 t) & \frac{\gamma_2}{2}\cos(\gamma_2 t) & \frac{1}{10} & \frac{\gamma_1}{3}\cos(\gamma_1 t) & 0 & 0\end{bmatrix}^T$$
$$\ddot{\boldsymbol{q}}^r = -\begin{bmatrix}\frac{\gamma_1^2}{2}\cos(\gamma_1 t) & \frac{\gamma_2^2}{2}\sin(\gamma_2 t) & 0 & \frac{\gamma_1^2}{3}\sin(\gamma_1 t) & 0 & 0\end{bmatrix}^T \tag{57}$$

where $\gamma_1 = 0.4\pi, \gamma_2 = \pi$. The EE was resting at the origin of the inertial frame $\{0\}$, i.e., $\boldsymbol{q}_0 = \dot{\boldsymbol{q}}_0 = \ddot{\boldsymbol{q}}_0 = \boldsymbol{0}$. Hence, the EE also had a large position error initially. However, the position and orientation errors converged to $\|\boldsymbol{e}_p\| < 2$ mm $\|\boldsymbol{e}_r\| < 2(10^{-3})$ rad, respectively, for $t > 2$ s. The error plots are displayed in Fig. 17.

B. MBFL Control

In general, tension control of CDPRs is challenging as it requires fast operating frequency and accurate tension feedback of the cables. Furthermore, an accurate model and state feedback is also required for the proposed tension scheme in Section VI-A. However, for D-CDPRs, this must include the state of the beam,

which is challenging to measure in practice. This makes the realization of direct closed-loop tension control from Section VI-A impractical.

To address these challenges, a practical and novel MBFL control approach is proposed. The MBFL uses cable lengths in order to produce the desired tension from the ID (42) using the computed-torque control accelerations (53) and (54). Most importantly, the MBFL control exploits a unique property of the deforming frame of D-CDPRs.

Theorem 1: If the beam of a planar D-CDPR has only one exit point, the length and the tension of each cable are uniquely related.

Hence, the D-CDPR model allows the desired cable tensions to be expressed uniquely with respect to the cable lengths. In other words, the cable length command could be used to produce desired tensions.

Proof: Consider a planar D-CDPR with a point mass EE. The ith cable is the only cable that attached to the jth deforming beam with stiffness k_j. Without loss of generality, the beam frame $\{B_j\}$ is overlapping with the inertial frame $\{0\}$. Hence, the y-component of the exit point, a_{iy} is a constant and x-component is a function of ith cable tension $a_{ix}(\tau_i)$ and $a_{ix}(0) = 0$. Under this setting

$$k_j a_{ix} = \tau_i \hat{w}_{ix} = \tau_i \frac{c_{ix}}{\|\boldsymbol{c}_i\|} \tag{58}$$

where c_{ix} is the x component of the ith cable vector. It is related to its y-component c_{iy} by

$$c_{ix} = \sqrt{\|\boldsymbol{c}_i\|^2 - c_{iy}^2}. \tag{59}$$

By rearranging the symbol

$$\tau_i^2 = \frac{k_j^2 a_{ix}^2}{c_{ix}^2}\|\boldsymbol{c}_i\| = \frac{k_j^2 (q_x - c_{ix})^2}{c_{ix}^2}\|\boldsymbol{c}_i\|. \tag{60}$$

Substituting (59) into (60) constructs the relationship between cable length and tension

$$\tau_i = k_j \|\boldsymbol{c}_i\| \left[\frac{|q_x|}{\sqrt{\|\boldsymbol{c}_i\|^2 - c_{iy}^2}} - 1 \right]. \tag{61}$$

$\|\boldsymbol{c}_i\| \geq |c_{iy}|$ as c_{iy} is the vertical component of $\boldsymbol{c}_i$. The derivative of (61) is given by

$$\frac{d\tau_i}{d\|\boldsymbol{c}_i\|} = -k_j \left[\frac{|q_x| c_{iy}^2}{(\|\boldsymbol{c}_i\|^2 - c_{iy}^2)^{3/2}} + 1 \right] < 0. \tag{62}$$

Hence, (61) is always decreasing and cable and tension are uniquely related within the defined range. ■

Corollary 1.1: If the beam of a spatial D-CDPR has only one exit point, the length and the tension of each cable are also uniquely related. This implies that for a D-CDPR with every cable attached to a single beam, the length command can be used to control the cable tensions directly.

Fig. 18 graphically describes this phenomena, where for a given pose, different cable tensions can be achieved by determining the corresponding lengths that will produce the desired frame bending. As the tension increases, the distance (also the cable length) between the exit point and the EE decreases. Fig. 19 illustrates the one-to-one relationship between the cable tension and length for the D-CDPR at three different fixed EE poses. This relation is plotted by decreasing the cable length to obtain the change in tension. For the sake of clarity, change of cable length is plotted such that $\Delta\|\boldsymbol{c}_i\|$ always starts at 0 for all cases. Due to the complex relationship between the D-CDPR frame's bending, cable lengths and cable tensions, analytical relationship between them could not be determined generally. Hence, the cable length command is instead determined using the D-CDPR FD model within the MBFL.

Fig. 20 shows the block diagrams of tension and MBFL control. The control scheme has an FD model and uses length command as input to the D-CDPR. A closed-loop length control could be setup via cable length feedback as it is less sensitive and can be readily obtained from sensors such as encoders. In the case of a D-CDPR with fixed exit points, this relationship

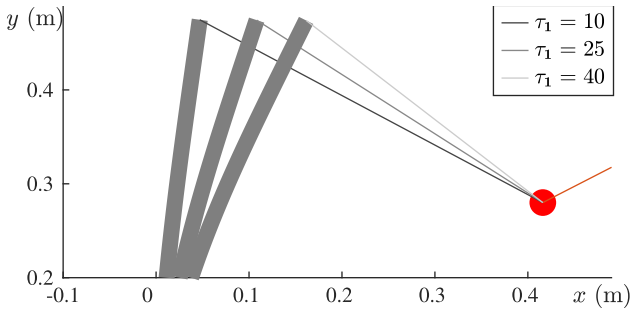

Fig. 18. Beam deflection due to different example cable tensions.

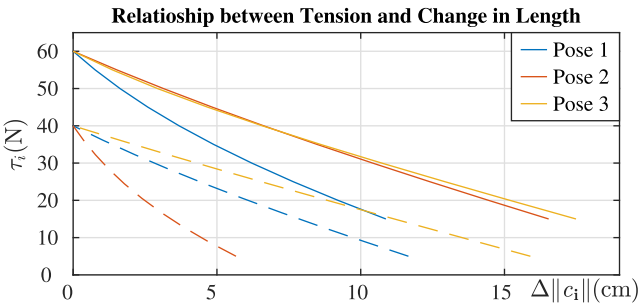

Fig. 19. Unique one to one relationship between the cable length and the cable tension of a D-CDPR at different pose. The solid line and dashed line are the tension-length relationship of cable 1 and 2, respectively.

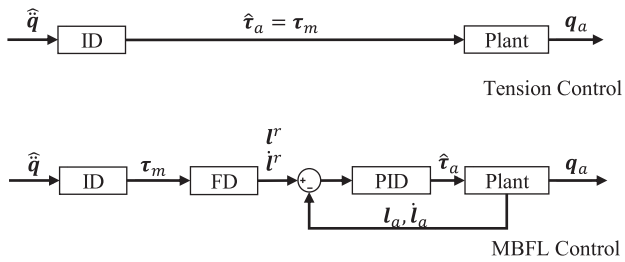

Fig. 20. Block diagrams of typical tension control versus MBFL.

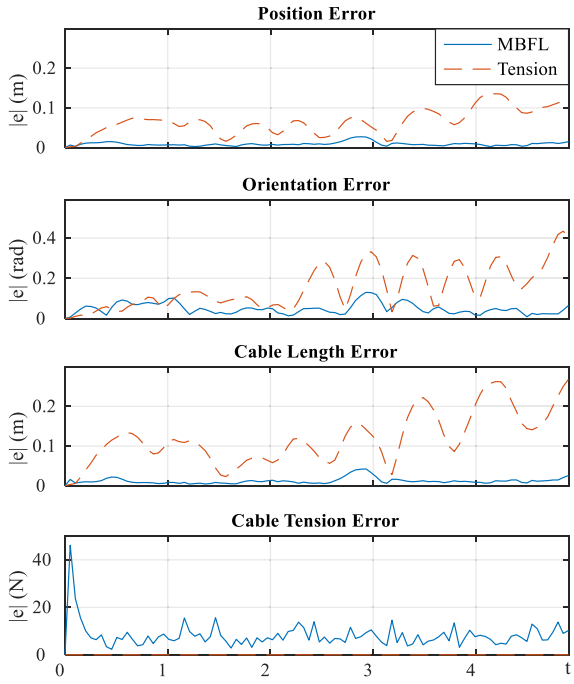

Fig. 21. Comparison of the errors of MBFL and tension control methods when random disturbance is applied to the EE.

does not hold. However, length control is still applicable to the D-CDPR, just as hybrid control is for CDPRs. Fig. 21 compares the tracking errors of MBFL and tension control. This was done over the circular trajectory defined in (56) as shown in Fig. 14. The MBFL results in a bounded task-space error. Because of geometric constraints, the tracking error plots of cable length and tension show that the length error is correlated to the EE position error. The open-loop tension control follows the reference tension command exactly (zero tension error shown in the last subplot), so it cannot reject the external disturbance acted on the EE and the error accumulates. Although there is potential for improving the tracking performance of the D-CDPR such as combining both tension and length control and by learning controls, this requires more extra sensors and computational power.

VII. Hardware Experiments

The proposed MBFL control strategy was tested on a 2-DoF suspended D-CDPR (the robot), which is identical to Fig. 10.

A. Robot Setup

The robot in Fig. 22 has two cables suspending a 1.68 kg EE. The cables were each connected to thin steel plate poles as the D-CDPR frame. Thin plate beams were selected to significantly reduce the bending stiffness that is coplanar to the robot's operating plane. Two identical beams have a height of 0.45 m and are 0.8 m apart. The beam's cross-section is a rectangle with dimensions of 30×2.5 mm. Two exit points are fixed to the beams' tops.

A calibration experiment was performed on the bending beams, where the beams were found to have a constant of $\mathrm{EI} = 7.5\ \mathrm{N} \cdot \mathrm{m}^2$. Within the deflection range of 0 to 120 mm at the exit point, both beams have a linear relationship between static deflection and load. As the beam deflection during the robot operation is always less than 120 mm, it is valid to use the EB beam model to model the bending beam.

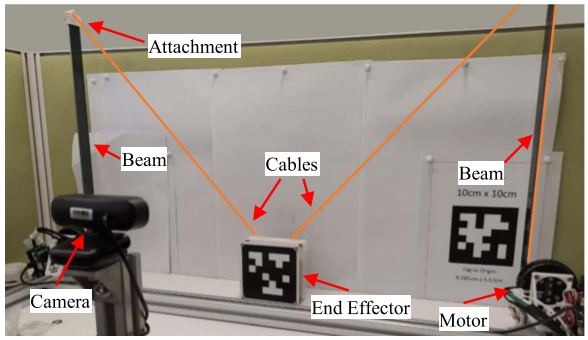

Fig. 22. Hardware setup of a 2-DoF deformable frame suspended cable robot.

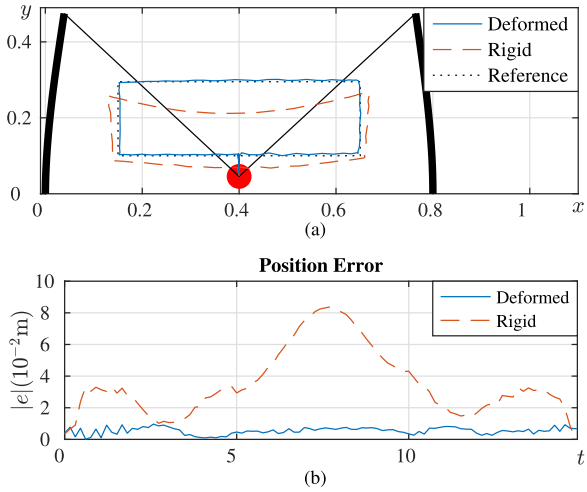

Fig. 23. Rectangular trajectory example comparing rigid frame and D-CDPR. (a) Overview of the tracking performance. (b) The position error of the EE.

An AprilTag [38] was attached to the EE to record the pose, as shown in Fig. 22. It was recorded at a frequency of 10 Hz by a camera. The location of the EE was calculated by comparing the transformation matrix between the reference frames of EE's AprilTag and stationary AprilTag (at the lower right corner of the setup).

B. Result

Two trajectories were tested on the hardware. The tracking performance of cable length was satisfactory because of PID control of the actuators within the MBFL control scheme, where the maximum cable length error $\|\boldsymbol{l}_a - \boldsymbol{l}^r\|$ was less than 5 mm.

1) Rectangular Trajectory: The first trajectory is a rectangle as shown as a dotted line in Fig. 23(a). Table IV lists the fixed points of the trajectory at various time instances T. The trajectory

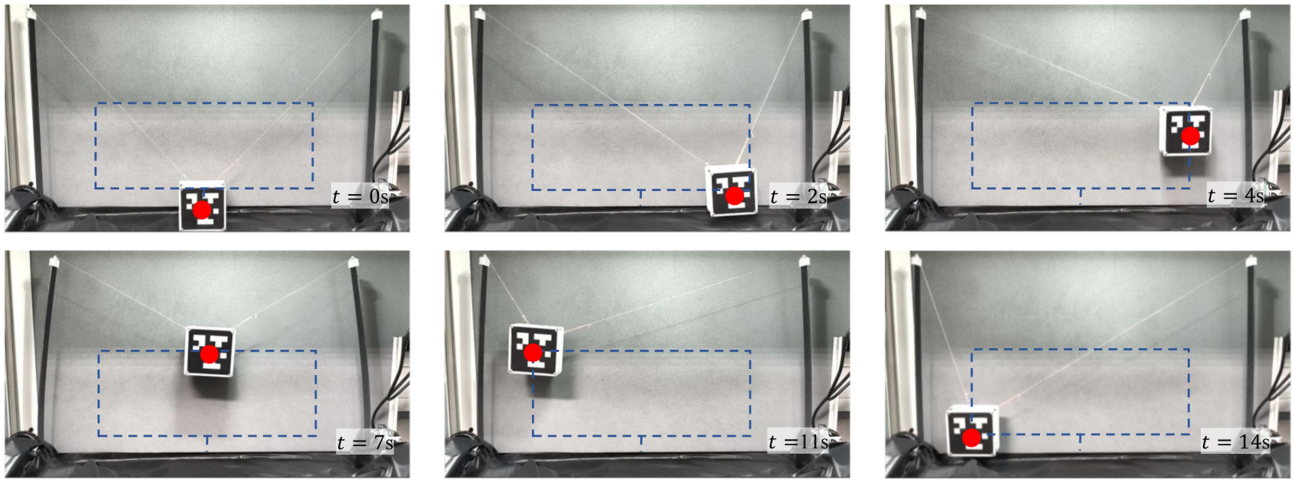

Fig. 24. Snapshots of the D-CDPR hardware that was running a rectangular trajectory. The red dot indicates the point mass EE.

TABLE IV
FIXED POINTS (IN METERS) OF THE RECTANGULAR TRAJECTORY

i	1	2	3	4	5	6	7	8
$\boldsymbol{q}_c^r(T_i)$	$\begin{bmatrix}0.40\\0.05\end{bmatrix}$	$\begin{bmatrix}0.40\\0.10\end{bmatrix}$	$\begin{bmatrix}0.65\\0.10\end{bmatrix}$	$\begin{bmatrix}0.65\\0.30\end{bmatrix}$	$\begin{bmatrix}0.15\\0.3\end{bmatrix}$	$\begin{bmatrix}0.15\\0.10\end{bmatrix}$	$\begin{bmatrix}0.40\\0.10\end{bmatrix}$	$\begin{bmatrix}0.40\\0.05\end{bmatrix}$
T_i	0 s	1 s	3 s	5 s	10 s	12 s	14 s	15 s

between each point is defined as

$$\begin{aligned}\boldsymbol{q}^r(t) &= \frac{t-T_i}{T_{i+1}-T_i}\left(\boldsymbol{q}^r(T_{i+1})-\boldsymbol{q}^r(T_i)\right)+\boldsymbol{q}^r(T_i)\\ \dot{\boldsymbol{q}}^r(t) &= \frac{\boldsymbol{q}^r(T_{i+1})-\boldsymbol{q}^r(T_i)}{T_{i+1}-T_i}\\ \ddot{\boldsymbol{q}}^r(t) &= \boldsymbol{0}.\end{aligned} \tag{63}$$

The bending frame model was used to calculate the first length command set, while the rigid frame model was used to calculate the second set. The tracking results are shown in Fig. 23(a) and (b). The EE's error when the rigid frame assumption was used was significantly larger. The maximum error is reduced to 10^{-2}m if the length command is obtained from the deformed frame.

Fig. 24 shows a series of snapshots of the D-CDPR hardware that was running a rectangular trajectory to demonstrate the proper motion of the D-CDPR EE, even under obvious deformation of the CDPR frame.

2) Hypotrochoid Trajectory: One more set of length command is tested on the robot. The majority of the trajectory is shaped like a flower. At the start ($t = 0$), the EE would travel a linear trajectory with total time of 3 s from the resting position to the start point of the hypotrochoid function. The hypotrochoid trajectory starts at $t_h = 0$ or $t = 3$, as defined by

$$\boldsymbol{q}^r(t_h) = \begin{bmatrix}\frac{1}{7}\left(\frac{3}{4}\cos\left(\frac{2}{3}t_h\right)+\cos t_h\right)\\ -\frac{3}{70}\sin\left(\frac{2}{3}t_h\right)+\frac{2}{35}\sin t_h\end{bmatrix}+\begin{bmatrix}0.4\\0.2\end{bmatrix}$$

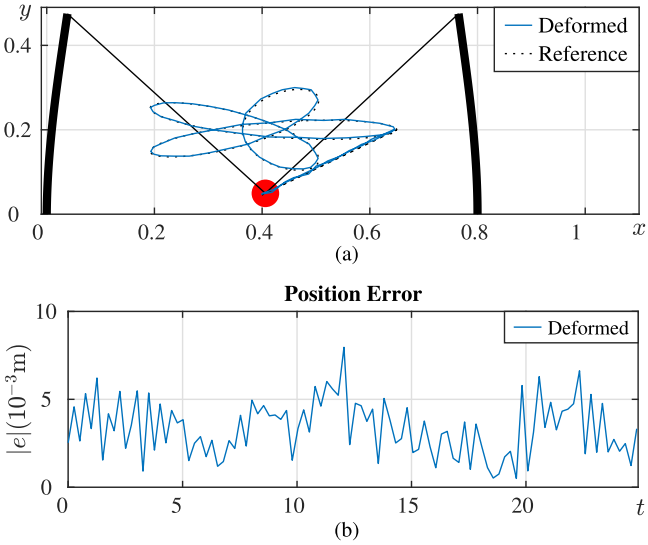

Fig. 25. Hypotrochoid trajectory example. (a) Overview of the tracking performance. (b) Position error of the EE.

$$\begin{aligned}\dot{\boldsymbol{q}}^r(t_h) &= \begin{bmatrix}\frac{1}{14}\left(\sin\left(\frac{2}{3}t_h\right)-2\sin t_h\right)\\ \frac{1}{35}\left(-2\cos\left(\frac{2}{3}t_h\right)+\cos t_h\right)\end{bmatrix}\\ \ddot{\boldsymbol{q}}^r(t_h) &= \begin{bmatrix}\frac{1}{21}\left(-\cos\left(\frac{2}{3}t_h\right)-3\cos t_h\right)\\ \frac{2}{105}\left(\sin\left(\frac{2}{3}t_h\right)-\frac{1}{3}\sin t_h\right)\end{bmatrix}\\ 0 &\le t_h \le 6\pi\end{aligned} \tag{64}$$

where $t_h = t - 3$. The EE was returned to the start point of the hypotrochoid function at $t_h = 6\pi$ or $t = 6\pi + 3$. To return to its resting position, the EE would move in a 3 s linear trajectory. As a result, the total travel time is $3 + 6\pi + 3 = 24.8$ s. The tracking results are shown in Fig. 25(a) and (b). The EE's error is about 10^{-2} m using the MBFL control scheme.

VIII. Conclusion

In this study, a generalized type of D-CDPR that allows for frame deformation of CDPRs is proposed. The main objectives of this research are to develop the model, conduct analysis, and implement practical controllers for D-CDPR. To address the long-standing drawback of CDPRs, cantilever beams were used as the building blocks of the frame due to their simplicity, cost-effectiveness, and ease of setup. The dynamic model of the D-CDPRs was presented, enabling the description of frame deformation and EE motion based on initial states and external forces. The SW of the D-CDPR was also analyzed, comparing it with that of traditional CDPRs. Furthermore, a unique model reference length command control was proposed and successfully implemented in the D-CDPR. Both simulation and robot hardware experiments demonstrated that the proposed control scheme exhibits disturbance and uncertainty rejection capabilities, along with satisfactory tracking performance. Future work will focus on the following:

1) the beam design and arrangement to better take advantage of flexible beam CDPRs;
2) different types of beam model, such as Timoshenko beams, can be used to consider larger deflections;
3) improving the tracking performance of the D-CDPR by developing new control approaches.

References

[1] X. Tang, "An overview of the development for cable-driven parallel manipulator," *Adv. Mech. Eng.*, vol. 6, 2014, Art. no. 823028.

[2] B. Zi, B. Duan, J. Du, and H. Bao, "Dynamic modeling and active control of a cable-suspended parallel robot," *Mechatronics*, vol. 18, no. 1, pp. 1–12, 2008.

[3] S. Qian, B. Zi, W.-W. Shang, and Q.-S. Xu, "A review on cable-driven parallel robots," *Chin. J. Mech. Eng.*, vol. 31, no. 1, pp. 1–11, 2018.

[4] J.-P. Merlet, *Parallel Robots*, vol. 128. Berlin, Germany: Springer, 2006.

[5] T. Heyden and C. Woernle, "Dynamics and flatness-based control of a kinematically undetermined cable suspension manipulator," *Multibody Syst. Dyn.*, vol. 16, no. 2, pp. 155–177, 2006.

[6] C. Gosselin, "Cable-driven parallel mechanisms: State of the art and perspectives," *Mech. Eng. Rev.*, vol. 1, no. 1, 2014, Art. no. DSM0004.

[7] R. L. Williams, J. S. Albus, and R. V. Bostelman, "3D cable-based cartesian metrology system," *J. Robot. Syst.*, vol. 21, no. 5, pp. 237–257, 2004.

[8] P. Miermeister et al., "The cablerobot simulator large scale motion platform based on cable robot technology," in *Proc. IEEE/RSJ Int. Conf. Intell. Robots Syst.*, 2016, pp. 3024–3029.

[9] J.-B. Izard et al., "On the improvements of a cable-driven parallel robot for achieving additive manufacturing for construction," in *Cable-Driven Parallel Robots*. Berlin, Germany: Springer, 2018, pp. 353–363.

[10] M. J. Varela, M. Ceccarelli, and P. Flores, "A kinematic characterization of human walking by using catrasys," *Mechanism Mach. Theory*, vol. 86, pp. 125–139, 2015.

[11] A. Pott, "An algorithm for real-time forward kinematics of cable-driven parallel robots," in *Advances in Robot Kinematics: Motion in Man and Machine*. Berlin, Germany: Springer, 2010, pp. 529–538.

[12] J.-P. Merlet, "Kinematics of the wire-driven parallel robot marionet using linear actuators," in *Proc. IEEE Int. Conf. Robot. Autom.*, 2008, pp. 3857–3862.

[13] A. Pott, "Influence of pulley kinematics on cable-driven parallel robots," in *Latest Advances in Robot Kinematics*. Berlin, Germany: Springer, 2012, pp. 197–204.

[14] L. Gagliardini, S. Caro, M. Gouttefarde, and A. Girin, "Discrete reconfiguration planning for cable-driven parallel robots," *Mechanism Mach. Theory*, vol. 100, pp. 313–337, 2016.

[15] D. Q. Nguyen, M. Gouttefarde, O. Company, and F. Pierrot, "On the analysis of large-dimension reconfigurable suspended cable-driven parallel robots," in *Proc. IEEE Int. Conf. Robot. Autom.*, 2014, pp. 5728–5735.

[16] A. Pott, *Cable-Driven Parallel Robots: Theory and Application*, vol. 120. Berlin, Germany: Springer, 2018.

[17] J. Pusey, A. Fattah, S. Agrawal, and E. Messina, "Design and workspace analysis of a 6–6 cable-suspended parallel robot," *Mechanism Mach. Theory*, vol. 39, no. 7, pp. 761–778, 2004.

[18] L. Gagliardini, S. Caro, M. Gouttefarde, P. Wenger, and A. Girin, "Optimal design of cable-driven parallel robots for large industrial structures," in *Proc. IEEE Int. Conf. Robot. Autom.*, 2014, pp. 5744–5749.

[19] I. B. Hamida, M. A. Laribi, A. Mlika, L. Romdhane, S. Zeghloul, and G. Carbone, "Multi-objective optimal design of a cable driven parallel robot for rehabilitation tasks," *Mechanism Mach. Theory*, vol. 156, 2021, Art. no. 104141.

[20] P. Bosscher, A. T. Riechel, and I. Ebert-Uphoff, "Wrench-feasible workspace generation for cable-driven robots," *IEEE Trans. Robot.*, vol. 22, no. 5, pp. 890–902, Oct. 2006.

[21] M. Gouttefarde, D. Daney, and J.-P. Merlet, "Interval-analysis-based determination of the wrench-feasible workspace of parallel cable-driven robots," *IEEE Trans. Robot.*, vol. 27, no. 1, pp. 1–13, Feb. 2011.

[22] Q. Duan and X. Duan, "Workspace classification and quantification calculations of cable-driven parallel robots," *Adv. Mech. Eng.*, vol. 6, 2014, Art. no. 358727.

[23] A. Alp and S Agrawal, "Cable suspended robots: Design, planning and control," in *Proc. IEEE Int. Conf. Robot. Autom.*, 2002, pp. 4275–4280.

[24] J. Lamaury, M. Gouttefarde, A. Chemori, and P.-E. Hervé, "Dual-space adaptive control of redundantly actuated cable-driven parallel robots," in *Proc. IEEE/RSJ Int. Conf. Intell. Robots Syst.*, 2013, pp. 4879–4886.

[25] H. Jamshidifar, S. Khosravani, B. Fidan, and A. Khajepour, "Vibration decoupled modeling and robust control of redundant cable-driven parallel robots," *IEEE/ASME Trans. Mechatron.*, vol. 23, no. 2, pp. 690–701, Apr. 2018.

[26] R. Bostelman et al., "Applications of the NIST robocrane," in *Proc. 5th Int. Symp. Robot. Manuf.*, 1994, pp. 403–410.

[27] S. Kawamura, W. Choe, S. Tanaka, and S. Pandian, "Development of an ultrahigh speed robot FALCON using wire drive system," in *Proc. IEEE Int. Conf. Robot. Automat.*, 1995, pp. 215–220.

[28] L. L. Cone et al., "Skycam: An aerial robotic camera system," *Byte*, vol. 10, 1985, Art. no. 122.

[29] R. Nan et al., "The five-hundred-meter aperture spherical radio telescope (FAST) project," *Int. J. Modern Phys. D*, vol. 20, no. 06, pp. 989–1024, 2011.

[30] B. Zi, J. Lin, and S. Qian, "Localization, obstacle avoidance planning and control of a cooperative cable parallel robot for multiple mobile cranes," *Robot. Comput.- Integr. Manuf.*, vol. 34, pp. 105–123, 2015.

[31] Z. Zake, N. Pedemonte, B. Moriniere, A. Suarez Roos, and S. Caro, "Elasto-static model and accuracy analysis of a large deployable cable-driven parallel robot," in *Proc. Int. Conf. Cable-Driven Parallel Robots*, 2023, pp. 381–393.

[32] L. Euler, *Methodus Inveniendi Lineas Curvas Maximi Minimive Proprietate Gaudentes Sive Solutio Problematis Isoperimetrici Latissimo Sensu Accepti*. Lausanne, Switzerland: Apud Marcum-Michaelem Bousquet & Socio, 1744.

[33] S. Bouchard, C. Gosselin, and B. Moore, "On the ability of a cable-driven robot to generate a prescribed set of wrenches," *ASME J. Mechanisms Robot.*, vol. 2, 2010, Art. no. 011010.

[34] M. Liu and D. G. Gorman, "Formulation of Rayleigh damping and its extensions," *Comput. Structures*, vol. 57, no. 2, pp. 277–285, 1995.

[35] C. Song and D. Lau, "Reference acceleration model predictive control (RA-MPC) for cable-driven robots," in *Proc. IEEE/RSJ Int. Conf. Intell. Robots Syst.*, 2022, pp. 11735–11742.

[36] R. H. Byrd, J. C. Gilbert, and J. Nocedal, "A trust region method based on interior point techniques for nonlinear programming," *Math. Program.*, vol. 89, pp. 149–185, 2000.

[37] S. L. Altmann, *Rotations, Quaternions, and Double Groups*. North Chelmsford, MA, USA: Courier Corporation, 2005.

[38] E. Olson, "AprilTag: A robust and flexible visual fiducial system," in *Proc. IEEE Int. Conf. Robot. Autom.*, 2011, pp. 3400–3407.

Arthur Ngo Foon Chan (Member, IEEE) received the B.Eng. (Hons.) and Ph.D. degrees in mechanical and automation engineering from the Chinese University of Hong Kong, Hong Kong, in 2017 and 2022, respectively.

His research interests include kinematics and dynamics modeling of cable-driven parallel manipulators, bending structure, and tensegrity robots.

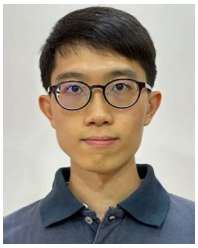

Wuichung Cheng (Graduate Student Member, IEEE) received the B.Eng. (Hons) degree in mechanical and automation engineering in 2020 from the Chinese University of Hong Kong, Hong Kong, where he is currently working toward the Ph.D. degree in mechanical and automation engineering.

His research interests include analysis and control of cable-driven parallel manipulators.

Darwin Lau (Senior Member, IEEE) received the B.Eng. (Hons) degree in mechatronics engineering, the B.C.S. degree in computer science, and the Ph.D. degree in mechanical engineering and robotics from the University of Melbourne, Parkville, VIC, Australia, in 2008 and 2014, respectively.

He was a Postdoctoral Research Fellow with Pierre and Marie Curie University, Paris, France, from 2014 to 2015. He is currently an Associate Professor with the Department of Mechanical and Automation Engineering, Chinese University of Hong Kong, Hong Kong. His research interests include kinematics, dynamics and control of redundantly actuated mechanisms, cable-driven parallel manipulators, construction and architectural robotics, and bioinspired robots.